The Astrophysical Journal, 841:71 (27pp), 2017 June 1 https://doi.org/10.3847/1538-4357/aa7069

Occurrence of Radio Minihalos in a Mass-limited Sample of Galaxy Clusters

Simona Giacintucci[1], Maxim Markevitch[2], Rossella Cassano[3], Tiziana Venturi[3], Tracy E. Clarke[1], and Gianfranco Brunetti[3]
[1] Naval Research Laboratory, 4555 Overlook Avenue SW, Code 7213, Washington, DC 20375, USA; simona.giacintucci@nrl.navy.mil
[2] NASA/Goddard Space Flight Center, Greenbelt, MD 20771, USA
[3] INAF—Istituto di Radioastronomia, via Gobetti 101, I-40129 Bologna, Italy
Received 2016 December 20; revised 2017 April 6; accepted 2017 April 28; published 2017 May 25

Abstract

We investigate the occurrence of radio minihalos—diffuse radio sources of unknown origin observed in the cores of some galaxy clusters—in a statistical sample of 58 clusters drawn from the *Planck* Sunyaev–Zel'dovich cluster catalog using a mass cut ($M_{500} > 6 \times 10^{14}\,M_{\odot}$). We supplement our statistical sample with a similarly sized nonstatistical sample mostly consisting of clusters in the ACCEPT X-ray catalog with suitable X-ray and radio data, which includes lower-mass clusters. Where necessary (for nine clusters), we reanalyzed the Very Large Array archival radio data to determine whether a minihalo is present. Our total sample includes all 28 currently known and recently discovered radio minihalos, including six candidates. We classify clusters as cool-core or non-cool-core according to the value of the specific entropy floor in the cluster center, rederived or newly derived from the *Chandra* X-ray density and temperature profiles where necessary (for 27 clusters). Contrary to the common wisdom that minihalos are rare, we find that almost all cool cores—at least 12 out of 15 (80%)—in our complete sample of massive clusters exhibit minihalos. The supplementary sample shows that the occurrence of minihalos may be lower in lower-mass cool-core clusters. No minihalos are found in non-cool cores or "warm cores." These findings will help test theories of the origin of minihalos and provide information on the physical processes and energetics of the cluster cores.

Key words: catalogs – galaxies: clusters: general – radio continuum: galaxies – surveys – X-rays: galaxies: clusters

1. Introduction

A striking feature of a number of galaxy clusters is the presence of diffuse synchrotron radiation in the form of large peripheral radio relics and two classes of centrally located radio sources—megaparsec-sized giant radio halos and smaller-scale minihalos (see Feretti et al. 2012 for a review). The importance of these extended, steep-spectrum[4] radio sources is nowadays widely recognized because their existence requires magnetic fields and ultrarelativistic electrons to be distributed throughout a large fraction of the cluster volume (e.g., Brunetti & Jones 2014).

Giant radio halos are associated with unrelaxed clusters (e.g., Cassano et al. 2010, 2013; Cuciti et al. 2015; Kale et al. 2015; Parekh et al. 2015; Yuan et al. 2015) without a central cool core (Rossetti et al. 2013), with a few possible outliers (Bonafede et al. 2014; Kale & Parekh 2016; Sommer et al. 2017). Minihalos, instead, are typically found in globally relaxed, cool-core clusters (e.g., Gitti et al. 2002; Govoni et al. 2009; Hlavacek-Larrondo et al. 2013; Giacintucci et al. 2014b; van Weeren et al. 2014; Kale et al. 2015; Yuan et al. 2015). Their emission envelops the central active radio galaxy, which is nearly always found at the center of a cool-core cluster (e.g., Mittal et al. 2009), and extends quite far from it ($r \sim 50$–300 kpc), typically filling the cluster cooling region. Minihalos are faint and usually quite amorphous in shape, and thus very different from typical extended radio galaxies with lobes and jets. Minihalos also differ from the dying radio galaxies that are sometimes found at the cluster centers, which have extended emission that typically has an ultrasteep radio spectrum ($\alpha_{\rm radio} \gtrsim 2$) and a morphology that somehow preserves the original lobed structure of the active phase, when the source was still fed by the central nucleus (e.g., Saikia & Jamrozy 2009; Murgia et al. 2011, 2012).

Minihalos often appear bounded by one or two X-ray cold fronts (Mazzotta & Giacintucci 2008; Giacintucci et al. 2014a, 2014b) that result from sloshing of the cool gas in the central core (e.g., Ascasibar & Markevitch 2006). Based on this coincidence, it has been proposed that minihalos arise from the reacceleration of seed relativistic electrons in the magnetized cool core (Gitti et al. 2002, 2004) by sloshing-induced turbulence (Mazzotta & Giacintucci 2008; ZuHone et al. 2013; Giacintucci et al. 2014a). Numerical simulations show that sloshing motions can amplify magnetic fields and develop turbulence in the area enclosed by the cold fronts, which may lead to the generation of diffuse radio emission confined to the sloshing region (ZuHone et al. 2013). A recent direct measurement of the gas velocities in the Perseus cool core with the *Hitomi* X-ray satellite revealed the presence of turbulence sufficient for the above scenario, and possibly for balancing the radiative cooling in the core (Hitomi Collaboration et al. 2016). An alternative explanation of minihalos is hadronic models (e.g., Pfrommer & Enßlin 2004; Fujita et al. 2007; Zandanel et al. 2014), where the radio-emitting electrons are generated through the interaction of cosmic-ray (CR) protons with the thermal protons in the intracluster medium. Both turbulence and CR protons should also contribute to balancing the radiative cooling in the cluster cores (e.g., Guo & Oh 2008; Fujita & Ohira 2011; Zhuravleva et al. 2014; Jacob & Pfrommer 2017a). Thus the relation between radio minihalos and cool cores may exist at a fundamental level (e.g., Fujita & Ohira 2013; Bravi et al. 2016), making these radio phenomena important for understanding the physics of cool cores.

The study of minihalos has been limited by their small number (e.g., Gitti et al. 2004; Cassano et al. 2008; Govoni et al. 2009),

[4] $\alpha_{\rm radio} > 1$, for $S_\nu \propto \nu^{-\alpha_{\rm radio}}$, where S_ν is the flux density at the frequency ν and $\alpha_{\rm radio}$ is the radio spectral index.

with only about 10 confirmed detections as of 2011 (Feretti et al. 2012). The number of known minihalos has then increased rapidly, with 22 confirmed detections[5] and six candidates to date (Hlavacek-Larrondo et al. 2013; Giacintucci et al. 2014b; van Weeren et al. 2014; Kale et al. 2015; Pandey-Pommier et al. 2016), including two new minihalos and one candidate detection that will be presented in a forthcoming paper (S. Giacintucci et al. 2017, in preparation, hereafter G17).

The new detections have allowed exploratory investigations of the statistical properties of minihalos and of their host clusters (Giacintucci et al. 2014b; Gitti et al. 2015; Kale et al. 2015; Yuan et al. 2015; Bravi et al. 2016; Jacob & Pfrommer 2017a, 2017b), which support the association of minihalos with relaxed, cool-core clusters. Furthermore, it has been noted that minihalos tend to be observed in the most massive and hottest clusters with cool cores (Giacintucci et al. 2014b). If true, this observation will provide a constraint to discriminate between different models for the origin of minihalos. In a broader context, it can provide information on the energy budget and physical processes in the cool cluster cores, where the radiative cooling is believed to be balanced by some nongravitational heating source(s) (e.g., McNamara & Nulsen 2007). The aim of the present work is to quantify this observation in a statistical way. For this purpose, we have selected a complete, mass-limited sample of 75 clusters from the *Planck* Sunyaev–Zel'dovich (SZ) cluster catalog (Planck Collaboration et al. 2014) and performed an X-ray and radio analysis of the majority of the sample members (77%) that have *Chandra* data. We complemented this *Chandra* statistical sample with a large additional sample of 48 clusters in the ACCEPT[6] X-ray catalog (Cavagnolo et al. 2009, hereafter C09), with suitable radio data, plus the Phoenix cluster (SPT-CL J2344-4243, McDonald et al. 2015), for a total of 106 clusters. Where necessary (for 27 clusters), we used the X-ray *Chandra* data to derive the profiles of gas density, temperature, and specific entropy. For those clusters in both samples without published radio observations on the angular scales of minihalos, we used archival Very Large Array (VLA) data to investigate the presence of a minihalo and present the results here (no minihalos were detected). We also include in our analysis the three new minihalo detections with the Giant Metrewave Radio Telescope that that will be presented in G17. We then compared the cluster mass and X-ray properties with the presence of a minihalo for our mass-limited as well as combined samples.

We adopt a ΛCDM cosmology with $H_0 = 70\,\mathrm{km\,s^{-1}\,Mpc^{-1}}$, $\Omega_m = 0.3$, and $\Omega_\Lambda = 0.7$. All errors are quoted at the 68% confidence level.

2. Definition of a Minihalo

To distinguish minihalos from other diffuse radio phenomena in clusters, such as radio galaxies (in active or dying phase), large radio halos, and relics, we use the following physically motivated definition. A minihalo is a diffuse radio source at the cluster center with the following properties:

1. The emission does not consist of radio lobes or tails, nor does it show, at any angular resolution, any morphological connection (jets) to the central active galactic nucleus (AGN) (such sources would be radio galaxies).
2. A minimum radius of approximately 50 kpc. At smaller radii, diffusion and other transport mechanisms, such as sloshing motions, can plausibly spread the relativistic electrons from the central AGN within their synchrotron radiative cooling time (e.g., see Section 6.4 in Giacintucci et al. 2014b) without the need for additional physics.
3. A maximum radius of $0.2R_{500}$.[7] This radius separates two physically distinct cluster regions. Based on X-ray and SZ observations, density, temperature, and pressure profiles of the thermal intracluster medium (ICM) outside this radius are self-similar, whereas a large scatter of the ICM profiles is observed at $r \lesssim 0.2R_{500}$ (e.g., McDonald et al. 2017 and references therein). This is caused by the increased importance of nongravitational processes such as cooling, AGN, and stellar feedback in the cores. Thus, diffuse radio emission that is confined within this radius can have a different origin, possibly related to processes in the core, from the emission on a larger scale (halos and peripheral relics). The bulk of the emission of large radio halos originates well outside $r = 0.2R_{500}$ (e.g., Cassano et al. 2007).

To determine whether a diffuse source fits the above definition we need radio data of a certain minimum quality. For item 1, we need sufficiently high resolution to image the range of scales from a few tens of kiloparsecs to a few kiloparsecs in order to determine the morphology of the central radio galaxy and rule out the possibility of the diffuse emission being part of it. It is also necessary to discriminate between genuine diffuse emission and a blend of individual radio galaxies in (or projected onto) the core and to remove their contribution as well as that of the central radio galaxy. At the same time, for items 2 and 3, sensitive, lower-resolution radio observations with a good sampling of the *uv* plane, particularly at short antenna spacings (that correspond to larger angular scales in the sky), are crucial to detect diffuse emission on a larger scale, including the scales beyond our adopted maximum size for the minihalo.

The size of the radio source that we use here is estimated as $R_{\rm radio} = \sqrt{R_{\rm max} R_{\rm min}}$, where $R_{\rm max}$ and $R_{\rm min}$ are the maximum and minimum radii of the 3σ surface brightness isocontour (Cassano et al. 2007). This obviously depends on the *uv* coverage of the data and the noise level of the image. As detailed in Section 3, a large fraction of the clusters in our statistical sample have already been reported to have either a large radio halo (well above $0.2R_{500}$) or a nondetection based on high-sensitivity images at low and high resolution, which is sufficient for our classification purpose. For the remaining clusters (except Perseus and Phoenix), which include all minihalos and ambiguous classifications from the literature, as well as clusters with no published radio images at the required resolution, we have uniformly analyzed new and archival radio data, with results presented in this paper (Section 6), Giacintucci et al. (2014b), and G17. The halo sizes come from those analyses. As shown in Appendices A and B, the data used for this paper, while heterogeneous, have sufficient sensitivity and a range of angular resolutions, as well

[5] The former minihalo in A2390 (Bacchi et al. 2003) is excluded because it was recently found to be larger (Sommer et al. 2017), borderline between giant halos (as defined in Cassano & Brunetti 2005) and minihalos. We note that this cluster has an unusually large cool core (Vikhlinin et al. 2005), comparable in size to the diffuse radio source.

[6] Archive of *Chandra* Cluster Entropy Profile Tables.

[7] R_{500} is the radius that encloses a mean overdensity of 500 with respect to the critical density at the cluster redshift.

Table 1
Statistical Sample

Planck Name PSZ1	Alternative Name	R.A.$_{J2000}$ (h, m, s)	Decl.$_{J2000}$ (deg, ′, ″)	z	M_{500} ($10^{14}\,M_{\odot}$)	R_{500} (Mpc)	Central Diffuse Radio Emission	R_{radio}/R_{500}	Radio References
Clusters with *Chandra* Observations									
G009.02−81.22	A2744	00 14 13.3	−30 22 31	0.307	$9.6^{+0.5}_{-0.5}$	1.35	halo	0.6	3, 4
G116.90−53.55	A68	00 36 57.7	+09 08 37	0.255	$6.2^{+0.6}_{-0.7}$	1.19	no detection	⋯	5
G106.84−83.24	A2813	00 43 27.4	−20 37 27	0.292	$9.2^{+0.5}_{-0.5}$	1.34	no detection	⋯	6
G212.97−84.04	A2895	01 18 10.8	−26 58 28	0.228	$6.1^{+0.5}_{-0.5}$	1.19	no detection	⋯	6
G159.81−73.47	A209	01 31 53.4	−13 34 27	0.206	$8.2^{+0.4}_{-0.4}$	1.33	halo	0.4	7, 8
G138.35−39.80	RXC J0142.0+2131	01 42 11.6	+21 32 32	0.280	$6.1^{+0.8}_{-0.8}$	1.17	no detection	⋯	9
G210.08−60.96	MACS J0257.6−2209	02 57 40.3	−22 09 46	0.322	$7.2^{+0.7}_{-0.7}$	1.22	halo (c)	⋯	10, 11
G164.20−38.90	A401	02 58 54.8	+13 32 24	0.074	$6.8^{+0.3}_{-0.3}$	1.31	halo	0.3	2, 12
G223.91−60.09	A3088	03 07 03.2	−28 40 24	0.254	$6.7^{+0.6}_{-0.6}$	1.22	no detection	⋯	8
G171.96−40.64	⋯	03 13 00.3	+08 22 53	0.270	$11.1^{+0.6}_{-0.6}$	1.44	halo	0.4	13
G182.42−28.28	A478	04 13 25.2	+10 28 19	0.088	$7.1^{+0.3}_{-0.4}$	1.32	minihalo	0.1	14
G208.80−30.67	A521	04 54 05.0	−10 13 35	0.248	$6.9^{+0.6}_{-0.6}$	1.24	halo	0.6	15, 16
G195.78−24.29	A520	04 54 15.9	+02 57 10	0.203	$7.1^{+0.6}_{-0.6}$	1.27	halo	0.4	17
G208.59−26.00	RXC J0510.7−0801	05 10 44.3	−08 01 12	0.220	$7.4^{+0.6}_{-0.6}$	1.28	bad data	⋯	5
G215.29−26.09	RXC J0520.7−1328	05 20 47.2	−13 30 08	0.336	$6.1^{+0.8}_{-0.8}$	1.15	bad data	⋯	18
G139.61+24.20	⋯	06 22 13.9	+74 41 39	0.267	$7.1^{+0.6}_{-0.6}$	1.24	minihalo (c)	0.04	2
G149.75+34.68	A665	08 30 50.9	+65 52 01	0.182	$8.2^{+0.4}_{-0.4}$	1.34	halo	0.5	19
G186.37+37.26	A697	08 42 59.6	+36 21 10	0.282	$11.5^{+0.5}_{-0.5}$	1.45	halo	0.4	20, 6, 7
G239.29+24.75	A754	09 08 56.2	−09 40 21	0.054	$6.7^{+0.2}_{-0.2}$	1.31	halo	0.5	21, 12, 22
G166.11+43.40	A773	09 18 04.5	+51 42 15	0.217	$7.1^{+0.4}_{-0.5}$	1.26	halo	0.4	3
G195.60+44.03	A781	09 20 16.0	+30 29 56	0.295	$6.4^{+0.6}_{-0.6}$	1.18	halo (c)	0.4	23, 24
G135.03+36.03	RBS 797	09 47 00.2	+76 23 44	0.345	$6.3^{+0.6}_{-0.7}$	1.16	minihalo	0.1	2, 25, 26
G266.85+25.06	A3444	10 23 54.8	−27 17 09	0.254	$7.6^{+0.5}_{-0.6}$	1.27	minihalo	0.1	2, 1, 5, 6
G149.21+54.17	A1132	10 58 25.9	+56 48 09	0.137	$6.2^{+0.3}_{-0.3}$	1.24	no detection	⋯	19
G257.13+55.63	RXC J1115.8+0129	11 15 54.9	+01 29 56	0.350	$6.4^{+0.7}_{-0.7}$	1.16	minihalo (c)	⋯	27
G278.58+39.15	A1300	11 31 55.8	−19 55 42	0.308	$8.8^{+0.6}_{-0.6}$	1.31	halo	0.4	4, 28, 29
G139.17+56.37	A1351	11 42 24.5	+58 31 41	0.322	$7.1^{+0.5}_{-0.5}$	1.21	halo	0.4	30, 7
G180.56+76.66	A1423	11 57 19.9	+33 36 39	0.214	$6.1^{+0.5}_{-0.5}$	1.20	no detection	⋯	6
G229.70+77.97	A1443	12 01 21.1	+23 06 31	0.269	$7.7^{+0.5}_{-0.6}$	1.27	halo	0.5	31
G289.19+72.19	RXC J1234.2+0947	12 34 31.8	+09 46 23	0.229	$6.0^{+0.6}_{-0.6}$	1.19	halo (c)	0.3	5
G114.99+70.36	A1682	13 06 54.9	+46 31 33	0.226	$6.2^{+0.4}_{-0.5}$	1.20	halo (c)	0.4	32, 4, 33
G313.33+61.13	A1689	13 11 26.5	−01 20 11	0.183	$8.9^{+0.4}_{-0.4}$	1.38	halo	0.5	2, 34
G323.30+63.65	A1733	13 27 00.7	+02 12 14	0.259	$7.1^{+0.6}_{-0.7}$	1.24	no data	⋯	⋯
G107.14+65.29	A1758a	13 32 39.5	+50 32 47	0.280	$8.0^{+0.4}_{-0.5}$	1.28	halo	0.6	4,7
G092.67+73.44	A1763	13 35 18.1	+41 00 10	0.228	$8.3^{+0.4}_{-0.4}$	1.32	no detection	⋯	6
G340.37+60.57	A1835	14 01 02.7	+02 51 56	0.253	$8.5^{+0.5}_{-0.6}$	1.32	minihalo	0.18	2, 35
G067.19+67.44	A1914	14 26 03.9	+37 49 35	0.171	$7.0^{+0.4}_{-0.4}$	1.28	halo	0.5	12
G340.94+35.10	AS 780	14 59 30.4	−18 08 58	0.236	$7.7^{+0.6}_{-0.6}$	1.29	minihalo	0.04	5, 2, 8
G355.07+46.20	RXC J1504.1−0248	15 04 05.4	−02 47 54	0.215	$7.0^{+0.6}_{-0.6}$	1.26	minihalo	0.11	36
G006.45+50.56	A2029	15 10 50.8	+05 44 43	0.077	$6.8^{+0.2}_{-0.2}$	1.30	minihalo	0.19	2, 35
G346.61+35.06	RXC J1514.9−1523	15 15 00.4	−15 21 29	0.223	$8.3^{+0.5}_{-0.6}$	1.33	halo	0.5	37
G044.24+48.66	A2142	15 58 25.6	+27 14 25	0.089	$8.8^{+0.3}_{-0.3}$	1.42	halo	0.3	38, 39
G006.76+30.45	A2163	16 15 49.2	−06 09 09	0.203	$16.4^{+0.4}_{-0.4}$	1.68	halo	0.7	40
G021.10+33.24	A2204	16 32 47.8	+05 35 32	0.151	$8.0^{+0.4}_{-0.4}$	1.34	minihalo	0.04	14
G097.72+38.13	A2218	16 35 52.0	+66 11 44	0.171	$6.4^{+0.3}_{-0.3}$	1.24	halo	0.3	2, 19
G072.61+41.47	A2219	16 40 18.6	+46 41 55	0.228	$11.0^{+0.4}_{-0.4}$	1.45	halo	0.6	12
G110.99+31.74	A2256	17 04 08.1	+78 38 07	0.058	$6.3^{+0.2}_{-0.2}$	1.28	halo	0.4	41, 42
G049.22+30.84	RXC J1720.1+2637	17 20 12.6	+26 37 23	0.164	$6.3^{+0.4}_{-0.4}$	1.24	minihalo	0.1	43
G055.58+31.87	A2261	17 22 21.9	+32 07 58	0.224	$7.4^{+0.4}_{-0.5}$	1.28	halo	0.4	44
G094.00+27.41	CL 1821+643	18 22 00.4	+64 20 34	0.332	$6.3^{+0.4}_{-0.4}$	1.16	halo	0.4	45, 46
G018.54−25.70	RXC J2003.5−2323	20 03 32.3	−23 23 30	0.317	$7.5^{+0.6}_{-0.7}$	1.24	halo	0.7	47
G053.42−36.25	MACS J2135.2−0102	21 35 10.1	−01 03 15	0.330	$7.6^{+0.6}_{-0.6}$	1.24	no data	⋯	⋯
G055.95−34.87	A2355	21 35 13.6	+01 25 40	0.231	$6.9^{+0.5}_{-0.5}$	1.24	no data	⋯	⋯
G073.98−27.83	A2390	21 53 44.0	+17 41 35	0.233	$9.5^{+0.4}_{-0.4}$	1.38	halo	0.3	44
G073.85−54.94	A2537	23 08 28.1	−02 12 00	0.297	$6.2^{+0.6}_{-0.7}$	1.17	no detection	⋯	6

Table 1
(Continued)

Planck Name PSZ1	Alternative Name	R.A.$_{J2000}$ (h, m, s)	Decl.$_{J2000}$ (deg, ′, ″)	z	M_{500} ($10^{14}\,M_{\odot}$)	R_{500} (Mpc)	Central Diffuse Radio Emission	R_{radio}/R_{500}	Radio References
G081.01−50.92	A2552	23 11 36.3	+03 38 38	0.300	$7.5^{+0.6}_{-0.6}$	1.25	halo (c)	0.3	5
G087.03−57.37	A2631	23 37 43.7	+00 16 06	0.278	$7.0^{+0.6}_{-0.6}$	1.23	no detection	–⋯	6
G034.03−76.59	A2667	23 51 38.3	−26 04 45	0.226	$6.8^{+0.5}_{-0.5}$	1.24	minihalo	0.05	2
Clusters without *Chandra* Observations									
G092.10−66.02	A2697	00 03 05.5	−06 05 26	0.232	$6.0^{+0.6}_{-0.6}$	1.19	no detection	⋯	8
G110.08−70.23	A56	00 34 01.6	−07 47 45	0.300	$6.2^{+0.7}_{-0.7}$	1.17	no data	⋯	⋯
G114.34−60.16	RXC J0034.4+0225	00 34 23.6	+02 25 14	0.350	$6.5^{+0.7}_{-0.8}$	1.17	no data	⋯	⋯
G142.18−53.27	A220	01 37 22.0	+07 52 31	0.330	$6.7^{+0.8}_{-0.9}$	1.19	no data	⋯	⋯
G222.97−65.69	A3041	02 41 27.6	−28 38 51	0.232	$6.1^{+0.5}_{-0.6}$	1.19	no data	⋯	⋯
G205.07−62.94	⋯	02 46 27.6	−20 32 05	0.310	$7.4^{+0.6}_{-0.7}$	1.24	no detection	⋯	48
G176.25−52.57	A384	02 48 13.1	−02 14 21	0.236	$6.4^{+0.6}_{-0.6}$	1.21	no data	⋯	⋯
G172.93+21.31	⋯	07 07 37.2	+44 19 23	0.331	$6.1^{+0.8}_{-0.8}$	1.15	no data	⋯	⋯
G169.64+33.84	⋯	08 16 42.5	+49 31 48	0.347	$6.2^{+0.8}_{-0.9}$	1.15	no data	⋯	⋯
G227.55+54.88	ZwCl 1028.8+1419	10 31 21.1	+14 06 19	0.305	$6.1^{+0.7}_{-0.7}$	1.16	no data	⋯	⋯
G288.26+39.94	RXC J1203.2−2131	12 03 14.4	−21 33 02	0.192	$7.3^{+0.5}_{-0.5}$	1.28	no data	⋯	⋯
G304.76+69.84	⋯	12 53 58.8	+06 58 40	0.346	$6.2^{+0.7}_{-0.8}$	1.15	no data	⋯	⋯
G309.46+37.32	RXC J1314.4−2515	13 14 23.1	−25 15 09	0.244	$6.2^{+0.7}_{-0.7}$	1.19	halo	0.3	8, 49
G068.32+81.81	RXC J1322.8+3138	13 22 48.0	+31 39 06	0.308	$6.6^{+0.6}_{-0.6}$	1.19	no data	⋯	⋯
G019.12+31.23	⋯	16 36 29.4	+03 08 51	0.280	$7.1^{+0.6}_{-0.7}$	1.23	no data	⋯	⋯
G049.83−25.22	RXC J2051.1+0216	20 51 20.3	+02 16 40	0.321	$6.1^{+0.7}_{-0.7}$	1.15	no data	⋯	⋯
G084.20−35.49	A2472	22 42 20.6	+17 29 17	0.314	$6.2^{+0.7}_{-0.8}$	1.16	no data	⋯	⋯

Note. Column 1: *Plank* cluster name. Column 2: alternative name. Columns 3–6: cluster coordinates, redshift, and mass from Planck Collaboration et al. (2014). Column 7: R_{500}, derived from M_{500}. Column 8: type of diffuse radio emission at the cluster center (c indicates a candidate detection). As defined in Section 2, sources with $R_{radio} \leqslant 0.2R_{500}$ are classified as minihalos. Column 9: radius of the central diffuse radio source, as defined in Section 2, in units of R_{500}. Column 10: radio references. If more than one reference is given, the first one is the reference for the image used to measure the radio size. Reference code: (1) this work, (2) G17, (3) Govoni et al. (2001), (4) Venturi et al. (2013), (5) Kale et al. (2015), (6) Venturi et al. (2008), (7) Giovannini et al. (2009), (8) Venturi et al. (2007), (9) Kale et al. (2013), (10) T. Venturi et al. (2017, in preparation), (11) A. Bonafede et al. (2017, private communication), (12) Bacchi et al. (2003), (13) Giacintucci et al. (2013), (14) Giacintucci et al. (2014b), (15) Brunetti et al. (2008), (16) Dallacasa et al. (2009), (17) Vacca et al. (2014), (18) Macario et al. (2014), (19) Giovannini & Feretti (2000), (20) Macario et al. (2011), (21) Macario et al. (2011), (22) Kassim et al. (2001), (23) Govoni et al. (2011), (24) Venturi et al. (2011a), (25) Gitti et al. (2006), (26) Doria et al. (2012), (27) Pandey-Pommier et al. (2016), (28) Reid et al. (1999), (29) Parekh et al. (2017), (30) Giacintucci et al. (2009a), (31) Bonafede et al. (2015), (32) Venturi et al. (2011b), (33) Macario et al. (2013), (34) Vacca et al. (2011), (35) Govoni et al. (2009), (36) Giacintucci et al. (2011b), (37) Giacintucci et al. (2011a), (38) Venturi et al. (2017), (39) Farnsworth et al. (2013), (40) Feretti et al. (2001), (41) Brentjens (2008), (42) Clarke & Ensslin (2006), (43) Giacintucci et al. (2014a), (44) Sommer et al. (2017), (45) Bonafede et al. (2014), (46) Kale & Parekh (2016), (47) Giacintucci et al. (2009b), (48) C. Ferrari et al. (2017, private communication), (49) Feretti et al. (2005).

as good sampling of short baselines in the *uv* plane, and thus would allow us to detect diffuse emission at the typical brightness on the core scale and, in most cases, at the larger scale of the giant halos. Furthermore, our measured minihalo sizes do not correlate with the signal-to-noise ratio of the radio images (Appendix B). This gives us assurance that the radio extent is not determined by the image sensitivity—the minihalos are intrinsically smaller than halos (see also Murgia et al. 2009). Of course, we cannot rule out the possibility that deeper data would uncover large-scale emission much fainter than the current radio halos in some of the sources that we classify here as minihalos. However, in a few very well-observed minihalos, we do see evidence for an abrupt drop of the radio brightness at a certain radius (Giacintucci et al. 2011, 2014a), which suggests that the extent of the minihalo has a physical significance.

3. Cluster Selection

To quantify the earlier observation that minihalos are found preferentially in massive cool-core systems (Giacintucci et al. 2014b), we use a combination of two samples in this paper. One is a statistically complete, mass-limited sample of massive clusters, while the other is a similarly sized arbitrary sample of clusters that do not satisfy some of the criteria for the complete sample, but do have high-quality radio and X-ray data and thus can increase the confidence of any correlations that we may find. The latter sample extends to lower masses, which is obviously helpful for investigating any correlation of the occurrence of minihalos with the cluster mass. As we will see, the *completeness* of the sample at lower masses is not critical for the conclusions of this work, while the completeness of the high-mass sample, used for the statistical analysis, is.

3.1. Statistical Sample

A complete, essentially mass-limited cluster sample can be extracted from the *Planck* SZ cluster catalog, since the total cluster SZ signal is a good proxy for the total mass (e.g., Nagai 2006). We selected all clusters with redshift $z \leqslant 0.35$, Galactic latitude $|b| \geqslant 20^{\circ}$, and the *Planck*-estimated total mass within R_{500} of $M_{500} > 6 \times 10^{14}\,M_{\odot}$. This mass cut is well above the

Table 2
Supplementary Sample

Cluster Name	*Planck* Name PSZ1	R.A.$_{J2000}$ (h, m, s)	Decl.$_{J2000}$ (deg, ′, ″)	z	M_{500} ($10^{14}\,M_{\odot}$)	R_{500} (Mpc)	Central Diffuse Radio Emission	R_{radio}/R_{500}	Radio References
Z348	⋯	01 06 50.3	+01 03 17	0.255	$2.5 \pm 0.3^{\star}$	0.88	no detection	⋯	3
A119	G125.68−64.12	00 56 14.5	−01 16 55	0.044	$3.34^{+0.22}_{-0.23}$	1.04	no detection	⋯	4
A141	G175.59−85.95	01 05 34.6	−24 38 00	0.230	$4.48^{+0.6}_{-0.73}$	1.08	no detection	⋯	3
A193	G136.90−53.31	01 24 59.4	+08 38 43	0.049	$1.8^{+0.27}_{-0.29}$	0.85	no detection	⋯	1
A267	G153.07−58.27	01 52 41.9	+00 58 01	0.227	$4.95^{+0.67}_{-0.72}$	1.11	no detection	⋯	3
MACS J0159.8-0849	G167.63−65.57	01 59 54.5	−08 50 14	0.405	$6.88^{+0.90}_{-0.98}$	1.16	minihalo	0.1	5, 2
A383	G177.64−53.52	02 47 46.5	−03 29 56	0.188	$4.47^{+0.60}_{-0.64}$	1.09	no detection	⋯	1
A399	G164.31−39.43	02 57 52.7	+13 04 11	0.072	$5.29^{+0.34}_{-0.35}$	1.20	halo	0.25	6
Perseus	⋯	03 19 47.2	+41 30 47	0.018	$6.1 \pm 0.6^{\star}$	1.28	minihalo	0.1	7, 8, 9
MACS J0329.6-0211	⋯	03 29 41.5	−02 11 46	0.450	$4.9 \pm 0.7^{\star}$	1.02	minihalo	0.1	2, 5
2A 0335+096	G176.30−35.06	03 38 44.4	+09 56 34	0.035	$2.27^{+0.24}_{-0.25}$	0.92	minihalo	0.1	2, 10
MACS J0417.5-1154	G205.94−39.46	04 17 36.2	−11 54 12	0.443	$11.70^{+0.64}_{-0.66}$	1.37	halo	0.3	11
MACS J0429.6-0253	⋯	04 29 36.0	−02 53 08	0.399	$4.1 \pm 0.8^{\star}$	0.98	no detection	⋯	1
RX J0439.0+0715	G189.52−25.10	04 39 01.2	+07 15 36	0.244	$5.75^{+0.70}_{-0.74}$	1.16	no detection	⋯	3
MS 0440.5+0204	⋯	04 43 09.7	+02 10 19	0.190	$5.0 \pm 1.2^{\star}$	1.13	no detection	⋯	1
A611	G184.70+28.92	08 01 01.7	+36 05 06	0.288	$5.85^{+0.60}_{-0.64}$	1.15	no detection	⋯	4
MS 0839.8+2938	⋯	08 42 55.9	+29 27 26	0.194	$3.4 \pm 0.5^{\star}$	1.00	no detection	⋯	1
Z2089	⋯	09 00 37.9	+20 54 58	0.235	$3.2 \pm 0.4^{\star}$	0.96	no detection	⋯	3, 4
ZwCl 2701	⋯	09 52 49.2	+51 53 05	0.214	$4.0 \pm 0.5^{\star}$	1.04	no detection	⋯	3, 4
A907	G249.38+33.27	09 58 22.2	−11 03 35	0.167	$5.18^{+0.47}_{-0.50}$	1.16	minihalo	0.05	2
ZwCL 3146	⋯	10 23 39.6	+04 11 10	0.291	$6.7 \pm 0.8^{\star}$	1.20	minihalo	0.07	12, 5
A1068	G179.13+60.14	10 40 48.7	+39 56 05	0.137	$3.55^{+0.38}_{-0.41}$	1.03	minihalo (c)	0.10	13
A1204	⋯	11 13 32.2	+17 35 40	0.171	$2.4 \pm 0.3^{\star}$	0.89	no detection	⋯	1
A1240	⋯	11 23 32.1	+43 06 32	0.159	$2.6 \pm 0.4^{\star}$	0.92	no detection	⋯	14
A1413	G226.19+76.78	11 55 19.4	+23 24 26	0.143	$5.98^{+0.38}_{-0.40}$	1.22	minihalo (c)	0.09	13
A1576	G125.72+53.87	12 36 48.9	+63 10 40	0.302	$5.98^{+0.48}_{-0.50}$	1.16	no detection	⋯	3
A1650	G306.71+61.04	12 58 45.6	−01 46 11	0.085	$4.00^{+0.34}_{-0.36}$	1.09	no detection	⋯	13
RX J1347.5−1145	G324.05+48.79	13 47 33.5	−11 45 42	0.452	$10.61^{+0.74}_{-0.77}$	1.32	minihalo	0.2	2, 15, 16
A1795	G033.84+77.17	13 48 55.0	+26 36 01	0.062	$4.54^{+0.21}_{-0.21}$	1.15	minihalo (c)	0.09	5
A1995	G096.87+52.48	14 52 56.4	+58 03 35	0.318	$5.15^{+0.49}_{-0.52}$	1.09	halo	0.3	17
MS 1455.0+2232	⋯	14 57 15.1	+22 20 34	0.258	$3.46 \pm 0.35^{\star}$	0.98	minihalo	0.1	2, 4, 18
A4	G053.52+59.52	15 10 12.6	+33 29 21	0.113	$4.92^{+0.35}_{-0.36}$	1.16	halo	0.3	17
RX J1532.9+3021	⋯	15 32 53.8	+30 20 58	0.363[a]	$4.7 \pm 0.6^{\star}$	1.04	minihalo	0.10	5, 3, 19
A2111	G054.99+53.42	15 39 34.9	+34 25 46	0.229	$5.46^{+0.60}_{-0.64}$	1.15	no detection	⋯	4
A2125	⋯	15 40 58.3	+66 18 28	0.247	$1.6 \pm 0.3^{\star}$	0.76	no detection	⋯	1
Ophiuchus	⋯	17 12 25.9	−23 22 33	0.028	$12.4 \pm 1.2^{\star}$	1.62	minihalo	0.15	2, 13, 20
A2255	G093.93+34.92	17 12 48.4	+64 04 03	0.081	$5.19^{+0.19}_{-0.19}$	1.19	halo	0.7	21, 22, 23
RX J1720.2+3536	G059.51+33.06	17 20 20.6	+35 37 42	0.387	$6.04^{+0.69}_{-0.74}$	1.12	minihalo (c)	0.18	24
ZwCl 1742.1+3306	G057.91+27.62	17 44 19.6	+32 59 19	0.076	$2.63^{+0.27}_{-0.29}$	0.95	uncertain	0.04	5
A2319	G075.71+13.51	19 21 09.6	+43 58 30	0.056	$8.59^{+0.22}_{-0.22}$	1.42	halo	0.4	25, 26, 27
MACS J1931.8–2634	G012.58−20.07	19 31 46.0	-26 33 51	0.352	$6.19^{+0.77}_{-0.83}$	1.15	uncertain	0.1	5, 28
RX J2129.6+0005	G053.65−34.49	21 29 42.5	+00 04 51	0.235	$4.24^{+0.55}_{-0.59}$	1.06	minihalo	0.08	12, 2
A2420	G046.48−49.42	22 10 12.9	−12 09 51	0.085	$4.48^{+0.26}_{-0.27}$	1.13	no detection	⋯	1
MACS J2228.5+2036	G083.30−31.01	22 28 29.1	+20 38 22	0.412	$7.82^{+0.71}_{-0.75}$	1.21	no detection	⋯	4, 11
MACS J2245.0+2637	⋯	22 45 04.7	+26 38 04	0.304	$4.8 \pm 0.8^{\star}$	1.07	no detection	⋯	29
A2556	⋯	23 13 00.9	−21 37 55	0.087	$2.4 \pm 0.2^{\star}$	0.92	no detection	⋯	1
A2626	⋯	23 36 30.3	+21 08 33	0.055	$2.4 \pm 0.5^{\star}$	0.93	uncertain	0.03	30
Phoenix[b]	⋯	23 44 42.2	−42 43 08	0.597	$12.6^{+2.0}_{-1.5}$	1.32	minihalo	0.17	31

Notes. Column 1: cluster name. Column 2: *Planck* name. Columns 3–5: cluster coordinates and redshift from Planck Collaboration et al. (2014) for the *Planck* clusters and from NASA/IPAC Extragalactic Database for the others. Column 6: cluster mass from Planck Collaboration et al. (2014). Values marked with * were estimated from the relation between M_{500} and T_X of Vikhlinin et al. (2009) using the core-excised temperatures in Table 6; errors were calculated from the temperature uncertainties and include statistical and systematic uncertainties for the M_{500}–T_X relation itself (Section 4). Column 7: R_{500}, derived from M_{500}. Column 8: type of diffuse radio emission at the cluster center (c indicates a candidate detection). As defined in Section 2, sources with $R_{radio} \leqslant 0.2R_{500}$ are classified as minihalos. Clusters marked as *uncertain* host central extended radio sources whose classification as a minihalo is uncertain; the radio size, morphology, and ultrasteep spectrum of these sources suggest that they could be instead dying/restarted radio galaxies (Section 3.2; Giacintucci et al. 2014b). Column 9: radius of the central diffuse radio source, as defined in Section 2, in units of R_{500}. Column 10: Radio references. If more than one reference is given, the first one is the reference for the image used to measure the radio size. Reference code: (1) this work, (2) G17, (3) Kale et al. (2013), (4) Venturi et al. (2008), (5) Giacintucci et al. (2014b), (6) Murgia et al. (2010b), (7) Sijbring (1993), (8) Burns et al. (1992), (9) Gendron-Marsolais et al. (2017), (10) Sarazin et al. (1995), (11) Parekh et al. (2017), (12) Kale et al. (2015), (13) Govoni et al. (2009), (14) Bonafede et al. (2009), (15) Gitti et al. (2007), (16) Ferrari et al. (2011), (17) Giovannini et al. (2009), (18) Mazzotta & Giacintucci (2008), (19) Hlavacek-Larrondo et al. (2013), (20) Murgia et al. (2010a), (21) Pizzo & de Bruyn (2009), (22) Govoni et al. (2005), (23) Feretti et al. (1997a), (24) Giacintucci et al. (2014a), (25) Storm et al. (2015), (26) Farnsworth et al. (2013), (27) Feretti et al. (1997b), (28) Ehlert et al. (2011), (29) T. Venturi et al. (2017, in preparation), (30) Gitti (2013), (31) van Weeren et al. (2014).

[a] Crawford et al. (1999).

[b] SPT-CL J2344-4243: coordinates, redshift, and mass are from McDonald et al. (2015) and references therein.

Table 3
Chandra Observations Analyzed in this Work

Cluster Name	Observation ID	Detector (ACIS)	Exposure (ks)	$N_{\rm H}$ (10^{20} cm^{-2})
A2813	9409	I	20.0	1.84*
A2895	9429	I	19.7	1.37*
RXC J0142.0+2131	10440	I	20.0	6.20*
A401	14024	I	111.5	$13.04^{+0.30}_{-0.30}$
A3088	9414	I	19.2	1.27*
PSZ1 G171.96-40.64	15302	I	25.9	$31.69^{+1.59}_{-1.57}$
RXC J0510.7-0801	14011	I	20.7	6.44*
PSZ1 G139.61+24.20	15139, 15297	I, I	17.9, 9.3	$13.11^{+1.7}_{-1.6}$
A781	15128	I	33.7	1.65*
A3444	9400	S	36.3	5.55*
A1132	13376	I	9.1	$8.52^{+1.9}_{-1.6}$
A1351	15136	I	32.9	0.98*
A1423	11724	I	25.7	1.81*
A1443	16279	I	18.9	$5.18^{+1.9}_{-1.4}$
RXC J1234.2+0947	11727	I	20.7	1.61*
A1682	11725	I	19.7	1.04*
A1689	6930, 7289	I, I	76, 75	$3.48^{+0.29}_{-0.29}$
A1733	11771	I	6.7	1.81*
AS 780	9428	S	39.4	7.39*
RXC J1504.1−0248	17197, 17669, 17670	I, I, I	29.8, 28.5, 44.6	$14.35^{+4.6}_{-4.6}$
RXC J1514.9−1523	15175	I	59.1	8.28*
A2142	5005, 15186	I, S	39.4, 87.1	$6.16^{+0.12}_{-0.12}$
CL 1821+643	9398	S	34.2	3.44*
RXC J2003.5−2323	7916	I	50.0	7.57*
MACS J2135.2−0102	11710	I	26.9	3.88*
A2355	15097	I	14.5	$8.98^{+2.41}_{-2.18}$
A2552	11730	I	22.8	4.60*
A2667	2214	S	9.3	1.73*
Z348	10465	S	48.7	2.50*
A141	9410	I	19.7	1.79*
Z2089	10463	S	40.4	2.88*
A1240	4961	I	51.8	2.85*
A1413	5002	I	37.1	1.83*
A1576	15127	I	28.8	1.08*
A1650	7242	I	37.6	1.35*
ZwCl 1742.1+3306	8267	I	7.8	3.83*
RX J2129.6+0005	9370	I	29.8	3.64*
A2420	8271	I	7.8	3.70*
A2626	3192	S	24.9	3.83*
Phoenix	16545	I	59.9	1.52*

Note. Column 1: cluster name. Column 2: observation identification number. Column 3: *Chandra* ACIS detector. Column 4: Total clean exposure. Column 5: column density of Galactic absorption adopted in this paper; values marked with * are from the Leiden/Argentine/Bonn radio survey (Section 5.3).

Planck completeness limit, and along with the z cut it is a compromise between the need to cover a range of cluster masses and the availability of the radio and X-ray data. We also imposed a cut in declination of Decl.$_{\rm J2000} \geqslant -30^{\circ}$ to ensure good visibility from the VLA and the Giant Metrewave Radio Telescope (GMRT), whose observations we use to investigate the presence of diffuse radio emission at the cluster center. Finally, we excluded the double cluster A115; its total mass inferred by *Planck* is $7.2 \times 10^{14}\,M_{\odot}$ (so above our mass limit), but based on optical and X-ray estimates of the cluster mass ratio (White et al. 1997; Barrena et al. 2007), the mass of each individual cluster falls below our mass threshold.

Our final *Planck* sample contains 75 clusters, listed in Table 1. This is essentially the same sample, apart from slightly different selection criteria, as that used by Cuciti et al. (2015) to study the occurrence of giant radio halos in clusters. *Chandra* X-ray observations are currently available for 58 (77%) of these clusters; hereafter we will refer to these clusters as the *Chandra* statistical sample. There are published accurate radio measurements available for 53 of these clusters (91%) from deep observations with the Westerbork Synthesis Radio Telescope (WSRT), VLA, and/or GMRT (Table 1), most of the latter taken as part of the GMRT Radio Halo Survey and its extension (Venturi et al. 2007, 2008; Kale et al. 2013, 2015). Two of the remaining clusters—RXC J0510.7–0801 and RXC J0520.7–1328—have pointed GMRT observations; however, the resulting images are not sensitive enough for us to investigate the presence of diffuse radio emission in these systems (Kale et al. 2015; Macario et al. 2014). We will see in Section 7 that these two clusters, along with those with no available radio data (A1733, MACS J2135.2-0102, and A2355), do not possess a cool

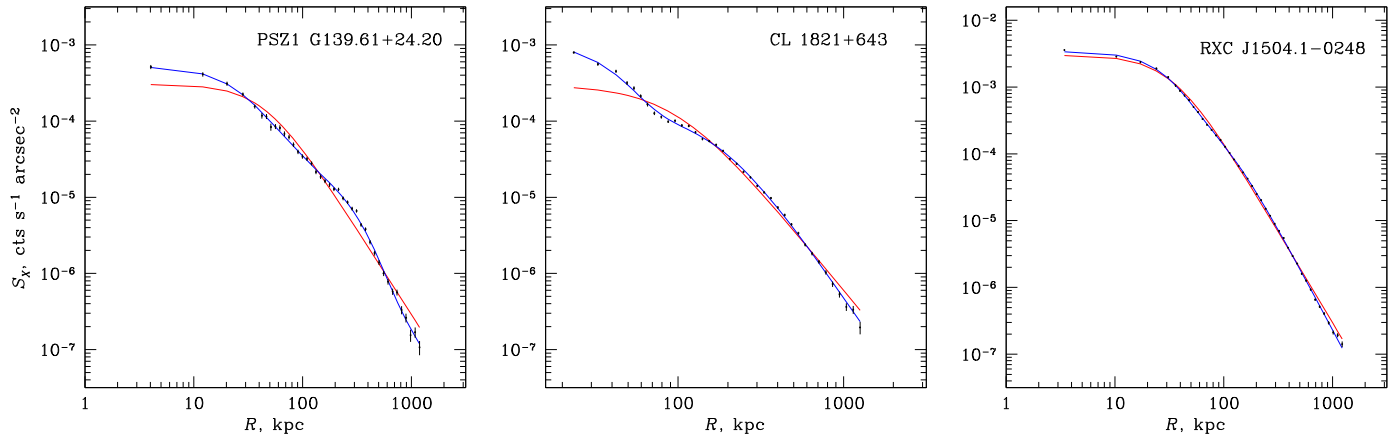

Figure 1. *Chandra* X-ray surface brightness profiles of PSZ1 G139.61+24.20, CL 1821+643, and RXC J1504.1–0248. Solid lines show the best-fit single (red) and double (blue) β-models.

Table 4
β-model Fits to the Gas Density Profile

Cluster Name	n_0 (10^{-3} cm^{-3})	r_{c1} (kpc)	β_1	r_{c2} (kpc)	β_2	f
A2895	5.6	212	0.7	...	...	0
RXC J0142.0+2131	16.1	32	0.6	212	0.7	0.50
A401	8.6	51	0.3	277	1.1	0.65
PSZ1G171.96−40.64	11.4	183	3.0	376	0.8	0.73
RXC J0510.7−0801	8.9	143	1.2	647	1.1	0.40
PSZ1 G139.61+24.20	77.3	22	0.5	804	3.0	0.03
A781	4.2	237	2.3	644	0.9	0.66
A3444	77.9	37	0.7	190	0.6	0.07
A1132	4.3	256	0.7	...	...	0
A1351	3.0	683	1.4	...	...	0
A1423	18.5	56	0.6	422	0.6	0.05
A1443	4.3	276	0.6	...	...	0
RXC J1234.2+0947	1.6	549	0.8	...	...	0
A1682	6.4	156	3.0	329	0.8	0.81
A1689	34.3	123	3.0	184	0.7	0.44
A1733	5.1	176	0.6	...	...	0
AS 780	86.5	21	0.5	...	...	0
RXC J1504.1−0248	170.2	68	3.0	75	0.7	0.41
RXC J1514.9−1523	2.0	592	0.8	...	...	0
A2142	27.6	90	3.0	139	0.6	0.81
CL 1821+643	80.5	86	3.0	186	0.7	0.18
RXC J2003.5−2323	2.2	698	1.0	...	...	0
MACS J2135.2−0102	5.6	191	0.6	...	...	0
A2355	2.1	615	1.0	...	...	0
A2552	18.1	54	0.7	238	0.7	0.40
Z348	75.2	33	0.7	...	...	0
Phoenix	209.4	34	0.6	...	...	0

Note. Column 1: cluster name. Columns 2–7: parameters of a β-model fit; see Equation (3). Fits were done out to R_{500} or as far in radius as the *Chandra* coverage allowed, which in all cases was far beyond the core region.

core, and the absence of radio information will not affect our main findings that are based on the cool-core part of the sample.

Our statistical sample (Table 1) contains 12 minihalos, of which nine are previously known and three—A2667, PSZ1 G139.61+24.2 (candidate), and RXC J1115.8+0129 (candidate)—are new detections. The former two are reported in the forthcoming paper G17 and the latter in Pandey-Pommier et al. (2016). The sample includes 26 radio-halo clusters and five candidates. Many of the clusters also contain peripheral radio relics, which is a distinct phenomenon (e.g., van Weeren et al. 2010) and we do not discuss it in this paper.

Among the 17 clusters in our *Planck* sample that do not have *Chandra* data (Table 1), 11 have *XMM-Newton* observations. However, most of them do not have high-sensitivity radio data at present. We inspected the *XMM-Newton* images and found that only three out of 11 can possibly have cool cores, and thus omitting them does not significantly affect our statistical conclusions.

3.2. Supplementary Sample

We supplement our statistical sample with 48 additional clusters drawn from ACCEPT, which includes clusters observed with *Chandra* as of 2008 and presents uniform X-ray analysis for them (C09), suitable for our work. The clusters were required to have deep, pointed VLA, WSRT, and GMRT observations in the literature and/or in the data archives (see Section 6), be at $z \leqslant 0.5$, Decl.$_{J2000} \geqslant -30°$, and have an average temperature of $kT > 3.5$ keV. This temperature cut corresponds to a lower total mass ($\sim 2 \times 10^{14}\,M_{\odot}$, based on a relation between M_{500} and T_X, Vikhlinin et al. 2009) than the lower limit of our statistical sample. To those clusters we add the Phoenix cluster ($z = 0.6$), which hosts the most distant minihalo found to date (van Weeren et al. 2014). This supplementary sample is given in Table 2. Twelve of these clusters possess a minihalo, including a recent GMRT detection in A907 (G17), and four host a candidate minihalo. The presence of a central diffuse radio source has been reported in three more clusters in this sample—ZwC 1742.1+3306, MACS J1931.8–2634 (Giacintucci et al. 2014b), and A2626 (Gitti 2013)—but their classification as minihalos is uncertain: the size (<50 kpc in A2626 and ZwC 1742.1+3306), radio morphology, and ultrasteep spectrum ($\alpha_{radio} \sim 2$) of these sources, as well as the possible association with X-ray cavities in MACS J1931.8–2634, suggest that they could instead be dying/restarted radio galaxies (Giacintucci et al. 2014b), whose aged emission, no longer fed by the central nucleus, is rapidly fading. For nine clusters with no published radio results on the angular scales of minihalos, we analyzed VLA archival observations (Section 6) and present the results here (no minihalos were detected among them).

Our final combined sample (statistical + supplementary) consists of 106 clusters and includes all 28 known minihalos, including six candidates.

Table 5
Best-fit Parameters for Temperature and Entropy Profiles

Cluster Name	T_0 (keV)	r_t (Mpc)	a	$T_{\rm min}/T_0$	$r_{\rm cool}$ (kpc)	$a_{\rm cool}$	K_0 (keV cm^2)	K_{100} (keV cm^2)	α	$r_{\rm max}$ (Mpc)
A2895	11.1	0.3	−0.3	1.0[a]	...	...	173 ± 65	106	1.0	1.4
RXC J0142.0+2131	7.5	1.9	0.0[a]	1.0[a]	...	...	131 ± 51	90	1.2	1.8
A401	7.9	3.1	0.0[a]	1.0[a]	...	...	180 ± 6	82	1.3	1.0
PSZ1G171.96−40.64	11.6	0.9	0.0[a]	1.0[a]	...	...	329 ± 74	42	1.4	2.0
RXC J0510.7−0801	9.2	1.0	0.0[a]	1.0[a]	...	...	158 ± 99	129	0.9	1.0
PSZ1 G139.61+24.20	13.8	0.4	0.0[a]	0.04	62	0.8	10 ± 10	186	1.1	0.1
A781	8.2	1.0	0.0[a]	1.0[a]	...	...	170 ± 36[b]	196	0.7	1.8
A3444	12.6	0.8	0.0[a]	0.31	299	1.1	18 ± 2	100	1.3	0.5
A1132	9.5	0.4	−0.33	1.0[a]	...	...	154 ± 31[b]	111	0.9	1.1
A1351	13.4	0.6	0.0[a]	1.0[a]	...	...	620 ± 93	3	2.6	1.3
A1423	9.7	0.6	−0.28	1.0[a]	...	...	27 ± 18	170	1.0	1.2
A1443	8.7	5.0	0.0[a]	1.0[a]	...	...	283 ± 57[b]	61	1.4	1.6
RXC J1234.2+0947	6.5	0.9	0.0[a]	1.0[a]	...	...	404 ± 93	23	1.3	1.2
A1682	10.4	0.4	−0.37	1.0[a]	...	...	143 ± 26[b]	139	1.0[a]	1.1
A1689	13.0	0.6	−0.16	1.0[a]	...	...	59 ± 4	109	1.7	0.1
AS 780	9.5	5.8	0.0[a]	0.37	146	3.2	19 ± 2	110	1.7	0.2
RXC J1504.1−0248	19.2	0.4	0.0[a]	0.15	348	1.0	11.1 ± 0.3	86	1.6	0.2
RXC J1514.9−1523	11.4	0.8	−0.10	1.0[a]	...	...	490 ± 108[b]	52	1.2	0.8
A2142	12.8	1.3	−0.21	1.0[a]	...	...	58 ± 2	127	1.2	1.0
CL 1821+643	9.5	5.0	0.0[a]	0.38	88	4.2	8 ± 5	125	1.3	0.2
RXC J2003.5−2323	17.6	0.4	0.0[a]	1.0[a]	...	...	708 ± 85	11	1.3[a]	1.1
MACS J2135.2-0102	12.4	0.7	−0.32	1.0[a]	...	...	142 ± 18	145	1.0	1.9
A2355	10.5	1.4	0.0[a]	1.0[a]	...	...	519 ± 117	57	1.3[a]	0.8
A2552	12.8	0.7	−0.21	1.0[a]	...	...	78 ± 33	164	1.0	1.6
Z348	4.7	0.6	0.0[a]	0.53	95	2.6	13 ± 1	73	1.7	0.2
Phoenix	32.6	0.4	0.0[a]	0.21	255	1.5	19 ± 3	123	1.7	0.3

Notes. Column 1: cluster name. Columns 2–7: best-fit parameters of the temperature fit; see Equation (4). Columns 8–10: best-fit parameters of the entropy fit (see Section 5.5 for details). Column 11: maximum radius used for the entropy fit.
[a] Fixed in the fit.
[b] Uncertainty from error in the first bin of the temperature profile.

4. Cluster X-Ray Properties

The purpose of this study is to quantify the occurrence of radio minihalos in clusters of different total masses with and without cool cores. To identify cool-core clusters in the sample, we follow C09 and use the specific entropy "floor" in the cluster centers. They find that the radial dependence of the specific entropy, defined in C09 and here as

$$K \equiv kTn_e^{-2/3}, \quad (1)$$

where T is the gas temperature and n_e is the electron number density, can be described, in the central cluster regions, as a function of radius, r, by

$$K(r) = K_0 + K_{100}\left(\frac{r}{100\ \rm kpc}\right)^{\alpha} \quad (2)$$

where K_0 is the so-called core entropy, K_{100} is a normalization for entropy at 100 kpc, and α is the power-law index.

Clusters with $K_0 < 30$–50 keV cm^2 (which represents a deep minimum of the entropy at the cluster center) invariably exhibit all the attributes of a cool core. For the cluster entropy profiles in the ACCEPT database, C09 combined projected gas temperatures with three-dimensional gas densities, which does not yield physically meaningful entropy values. However, their values serve our current purpose of identifying the cool cores well, and have been used for similar purposes in the literature. Therefore, for the present analysis, we chose to use the K_0 values from C09 for those clusters that already had high-quality *Chandra* data (81 out of 106 clusters in our combined sample), and to emulate the C09 derivation (with some technical differences) for the 27 clusters with new or significantly improved *Chandra* data that appeared since C09. This will be described in Section 5.5.

For total cluster masses, we use the *Planck* SZ-based estimates where available, otherwise we obtain a mass estimate from the M_{500}–$T_{\rm X}$ relation in Vikhlinin et al. (2009), using an X-ray measured, core-excised temperature. Estimates of M_{500}–$T_{\rm X}$ are required for 17 out of 48 clusters (35%) in the supplementary sample. Core-excised temperatures are taken from Cavagnolo et al. (2008, hereafter C08) if available, otherwise we derive them here (Section 5.4) in the same manner for uniformity. Errors for those masses are calculated from the statistical uncertainties on temperature and include statistical and systematic uncertainties for the M_{500}–$T_{\rm X}$ relation itself, as estimated by Vikhlinin et al. (2009).

5. *Chandra* Data Analysis

The ACCEPT sample of C09 contains clusters in the *Chandra* archive as of 2008. Since then, *Chandra* has observed new clusters, e.g., those in our statistical sample that were discovered by *Planck* (two clusters), and reobserved others, including several borderline clusters ("warm cores") for which it is important for us to have an accurate core temperature profile. Here, we have analyzed *Chandra* data for such new

Table 6
Temperatures and Core Entropies for the Statistical Sample

Cluster Name	$T_{X,ce}$ (keV)	K_0 (keV cm^2)	References	Cluster Name	$T_{X,ce}$ (keV)	K_0 (keV cm^2)	References
A2744	$9.2^{+0.7}_{-0.6}$	438 ± 59	2, 3	RXC J1234.2+0947	$5.7^{+0.4}_{-0.4}$	404 ± 93	1, 1
A68	$9.0^{+1.5}_{-1.1}$	217 ± 89	2, 3	A1682	$7.2^{+0.6}_{-0.5}$	143 ± 26	1, 1
A2813	$8.2^{+0.5}_{-0.5}$	268 ± 44	1, 3	A1689	$9.9^{+0.2}_{-0.2}$	59 ± 4	1, 1
A2895	$7.8^{+0.5}_{-0.5}$	173 ± 65	1, 1	A1733	$9.1^{+1.8}_{-1.3}$	332 ± 148[a]	1, 1
A209	$7.3^{+0.6}_{-0.5}$	106 ± 27	2, 3	A1758a	$12.1^{+1.2}_{-0.9}$	231 ± 37	2, 3
RXC J0142.0+2131	$7.1^{+0.6}_{-0.5}$	131 ± 51	1, 1	A1763	$7.8^{+0.7}_{-0.6}$	215 ± 33	2, 3
MACS J0257.6−2209	$8.0^{+1.1}_{-0.9}$	156 ± 25	2, 3	A1835 (MH)	$9.8^{+0.6}_{-0.5}$	11 ± 3	2, 3
A401	$7.8^{+0.6}_{-0.6}$	180 ± 6	1, 1	A1914	$9.6^{+0.6}_{-0.5}$	107 ± 18	2, 3
A3088	$9.6^{+0.7}_{-0.7}$	83 ± 8	1, 3	AS 780 (MH)	$7.1^{+0.3}_{-0.3}$	19 ± 2	1, 1
PSZ1G171.96−40.64	$11.0^{+0.9}_{-0.5}$	329 ± 74	1, 1	RXC J1504.1−0248 (MH)	$7.6^{+0.1}_{-0.1}$	11.1 ± 0.3	1, 1
A478 (MH)	$7.3^{+0.3}_{-0.2}$	8 ± 1	2, 3	A2029 (MH)	$8.2^{+0.3}_{-0.3}\star$	11 ± 1	2, 3
A521	$7.0^{+0.6}_{-0.5}$	260 ± 36	2, 3	RXC J1514.9−1523	$8.6^{+0.4}_{-0.3}$	490 ± 108	1, 1
A520	$9.3^{+0.7}_{-0.6}$	326 ± 29	2, 3	A2142	$8.8^{+0.1}_{-0.1}$	58 ± 2	1, 1
RXC J0510.7−0801	$8.4^{+0.5}_{-0.4}$	158 ± 99	1, 1	A2163	$19.2^{+0.9}_{-0.8}$	438 ± 83	2, 3
RXCJ 0520.7−1328	$6.4^{+0.8}_{-0.7}$	89 ± 22	2,3	A2204 (MH)	$8.7^{+0.6}_{-0.5}$	10 ± 1	2,3
PSZ1G139.61+24.20 (cMH)	$7.5^{+0.4}_{-0.4}$	10 ± 10	1,1	A2218	$7.3^{+0.4}_{-0.4}$	289 ± 20	2,3
A665	$7.5^{+0.4}_{-0.3}$	135 ± 24	2,3	A2219	$12.6^{+0.7}_{-0.6}\star$	412 ± 43	2,3
A697	$9.5^{+0.9}_{-0.8}$	167 ± 24	2,3	A2256	$5.7^{+0.2}_{-0.2}\star$	350 ± 12	2,3
A754	$10.0^{+0.3}_{-0.3}$	270 ± 24	4,3	RXC J1720.1+2637 (MH)	$6.4^{+0.3}_{-0.3}$	21 ± 2	2,3
A773	$7.8^{+0.7}_{-0.6}$	244 ± 32	2,3	A2261	$7.6^{+0.5}_{-0.4}$	61 ± 8	2,3
A781	$8.2^{+0.7}_{-0.6}$	170 ± 36	1,1	CL 1821+643	$9.5^{+0.4}_{-0.4}$	8 ± 5	1,1
RBS 797 (MH)	$7.7^{+0.9}_{-0.8}$	21 ± 2	2,3	RXC J2003.5−2323	$10.8^{+0.8}_{-0.6}$	708 ± 85	1,1
A3444 (MH)	$7.1^{+0.2}_{-0.2}$	18 ± 2	1, 1	MACS J2135.2−0102	$8.6^{+0.8}_{-0.6}$	142 ± 18	1, 1
A1132	$6.8^{+0.6}_{-0.5}$	154 ± 31	1, 1	A2355	$9.4^{+0.9}_{-0.9}$	519 ± 117	1, 1
RXC J1115.8+0129 (cMH)	$6.8^{+1.2}_{-0.9}$	23 ± 5	2, 3	A2390	$10.9^{+0.3}_{-0.3}$	15 ± 7	2, 3
A1300	$8.6^{+1.2}_{-1.0}$	97 ± 23	2, 3	A2537	$8.4^{+0.8}_{-0.7}$	110 ± 19	2, 3
A1351	$9.9^{+0.7}_{-0.7}$	620 ± 93	1, 1	A2552	$9.2^{+0.7}_{-0.7}$	78 ± 33	1, 1
A1423	$6.4^{+0.3}_{-0.3}$	27 ± 18	1, 1	A2631	$7.1^{+1.1}_{-0.8}$	309 ± 37	2, 3
A1443	$8.6^{+0.6}_{-0.4}$	283 ± 57	1, 1	A2667 (MH)	$7.3^{+0.4}_{-0.4}$	19 ± 3	1, 3

Note. Column 1: cluster name. The presence of a minihalo or a candidate is indicated by MH or cMH, respectively. Column 2: temperature within R_{2500} (R_{5000} for those clusters marked with $\star$) measured in the 0.7–7 keV band; the central $r = 70$ kpc region has been excised for all clusters except A754. Column 3: core entropy. Column 4: references for temperature and the core entropy floor, respectively: (1) this work, (2) C08, (3) C09, (4) Markevitch et al. (2003).
[a] From the temperature measured within the central $r = 120$ kpc.

clusters and important improvements. Seven of the new observations are part of the *Chandra* Visionary Program to study the X-ray properties of *Planck*-selected clusters, including the fraction of cool cores (Andrade-Santos et al. 2017).

We will use C08 and C09 entropy and temperature values for those clusters that have been reobserved but for which the old data were accurate enough. Updates of *Chandra* calibration since C08 and C09 have negligible effects for our current qualitative purposes.

5.1. Data Reduction and Image Preparation

The *Chandra* observations analyzed in this paper are listed in Table 3, which includes the observation identifiers, clean exposure times, and the adopted column density of Galactic absorption N_H (Section 5.3). The Level-1 ACIS event files from the archive were reprocessed following the procedure described in Vikhlinin et al. (2005) using the *Chandra* Calibration Database (CALDB) 4.6.3. Exclusion of time intervals with elevated background and background modeling were done as described in Markevitch et al. (2003). To model the detector and sky background, we used the blank-sky data sets from the CALDB appropriate for the date of each observation, normalized using the ratio of the observed to blank-sky count rates in the 9.5–12 keV band. Following Markevitch et al. (2000), we also subtracted the ACIS readout artifact, which is an important effect in the radial temperature profiles in the presence of a sharp brightness peak.

We used images in the 0.5–4 keV and 2–7 kev energy bands to detect the unrelated X-ray point sources and small-scale extended sources in each observation. These sources were masked from the image and spectral analysis. For each cluster, we need to extract and fit a radial surface brightness profile and a radial temperature profile.

5.2. Gas Density Profiles

For each cluster, we obtained a background-subtracted, exposure-corrected image in the 0.7–2 keV band. For clusters with multiple (typically offset) ACIS observations, we first coadded the individual background-subtracted images and then divided the images from counts by the sum of the corresponding exposure maps. We then extracted radial surface brightness profiles, centered on the cluster X-ray centroid.

While a simple spherically symmetric β-model for the gas density (Cavaliere & Fusco-Femiano 1978) is a reasonable

Table 7
Temperatures and Core Entropies for the Supplementary Sample

Cluster Name	$T_{X,ce}$ (keV)	K_0 (keV cm^2)	References	Cluster Name	$T_{X,ce}$ (keV)	K_0 (keV cm^2)	References
Z348	$3.9^{+0.1}_{-0.1}$	13 ± 1	1, 1	A1413 (cMH)	$8.3^{+0.2}_{-0.2}$	64 ± 8	1, 3
A119	$5.9^{+0.3}_{-0.3}\star$	234 ± 88	2, 3	A1576	$9.5^{+0.7}_{-0.7}$	186 ± 49	1, 3
A141	$7.2^{+0.6}_{-0.5}$	205 ± 27	1, 3	A1650	$6.1^{+0.1}_{-0.1}$	38 ± 10	1, 3
A193	$4.2^{+1.0}_{-0.6}$	186 ± 13	5, 3	RX J1347.5−1145 (MH)	$14.6^{+1.0}_{-0.8}$	13 ± 21	2, 3
A267	$6.7^{+0.6}_{-0.5}$	169 ± 18	2, 3	A1795 (cMH)	$6.1^{+0.2}_{-0.2}\star$	19 ± 1	2, 3
MACS J0159.8−0849 (MH)	$9.2^{+0.7}_{-0.6}$	19 ± 4	2, 3	A1995	$8.4^{+0.7}_{-0.6}$	374 ± 60	2, 3
A383	$4.9^{+0.3}_{-0.3}$	13 ± 2	2, 3	MS 1455.0+2232 (MH)	$4.8^{+0.1}_{-0.1}$	17 ± 2	2, 3
A399	$8.0^{+0.4}_{-0.3}$	153 ± 19	2, 3	A2034	$7.2^{+0.2}_{-0.2}$	233 ± 23	2, 3
Perseus (MH)	$6.4^{+0.1}_{-0.1}$	19.4 ± 0.2	4, 3	RX J1532.9+3021 (MH)	$6.0^{+0.4}_{-0.4}$	17 ± 2	2, 3
MACS J0329.6−0211 (MH)	$6.3^{+0.5}_{-0.4}$	11 ± 3	2, 3	A2111	$7.1^{+1.3}_{-1.0}$	107 ± 97	2, 3
2A 0335+096 (MH)	$3.6^{+0.1}_{-0.1}$	7.1 ± 0.1	5, 3	A2125	$2.9^{+0.3}_{-0.3}$	225 ± 32	2, 3
MACS J0417.5−1154	$11.1^{+2.0}_{-1.5}$	27 ± 7.3	2, 3	Ophiuchus (MH)	$10.3^{+0.2}_{-0.2}$	9 ± 1	4, 3
MACS J0429.6−0253	$5.7^{+0.6}_{-0.5}$	17 ± 4.3	2, 3	A2255	$6.1^{0.2}_{-0.2}$	529 ± 28	2, 3
RX J0439.0+0715	$5.6^{+0.4}_{-0.3}$	67 ± 19	2, 3	RX J1720.2+3536 (cMH)	$7.2^{+0.5}_{-0.5}$	24 ± 3	2, 3
MS 0440.5+0204	$6.0^{+0.9}_{-0.7}\star$	26 ± 8	2, 3	ZwCl 1742.1+3306 (u)	$4.4^{+0.2}_{-0.2}$	24 ± 2	1, 3
A611	$7.1^{+0.6}_{-0.5}$	125 ± 19	2, 3	A2319	$8.8^{+0.3}_{-0.2}$	270 ± 5	4, 3
MS 0839.8+2938	$4.7^{+0.3}_{-0.3}$	19 ± 3	2, 3	MACS J1931.8−2634 (u)	$7.0^{+0.7}_{-0.6}$	15 ± 4	2, 3
Z2089	$4.4^{+0.2}_{-0.2}$	24 ± 5	1, 3	RX J2129.6+0005 (MH)	$7.3^{+0.3}_{-0.3}$	21 ± 4	1, 3
ZwCl 2701	$5.2^{+0.3}_{-0.3}$	40 ± 4	2, 3	A2420	$6.6^{+0.2}_{-0.2}$	333 ± 68	1, 3
A907 (MH)	$5.6^{+0.2}_{-0.2}$	23 ± 3	2, 3	MACS J2228.5+2036	$7.9^{+1.1}_{-0.9}$	119 ± 39	2, 3
ZwCL 3146 (MH)	$7.5^{+0.3}_{-0.3}$	11 ± 2	2, 3	MACS J2245.0+2637	$6.1^{+0.6}_{-0.5}$	42 ± 7	2, 3
A1068 (cMH)	$4.7^{+0.2}_{-0.2}\star$	9 ± 1	2, 3	A2556	$3.6^{+0.2}_{-0.2}\star$	12 ± 1	2, 3
A1204	$3.6^{+0.2}_{-0.2}$	15 ± 1	2, 3	A2626 (u)	$3.6^{+0.1}_{-0.1}$	23 ± 3	1, 3
A1240	$4.4^{+0.3}_{-0.3}$	462 ± 42	1, 3	Phoenix (MH)	$12.9^{+0.7}_{-0.7}$	19 ± 3	1, 1

Note. Column 1: cluster name. The presence of a minihalo, a candidate minihalo, or a central diffuse source with uncertain classification (Section 3.2) is indicated by MH, cMH, or u respectively. Column 2: cluster global temperature within R_{2500} (R_{5000} for those clusters marked with $\star$) measured in the 0.7–7 keV band; the central $r = 70$ kpc region has been excised for all clusters except Perseus, 2A 0335+096, Ophiuchus, A193 and A2319. Column 3: core entropy. Column 4: references for temperature and the core entropy floor: (1) this work, (2) C08, (3) C09, (4) Ikebe et al. (2002), (5) David et al. (1993).

description for non-cool-core clusters, it does not describe cool cores well (e.g., Jones & Forman 1984). We therefore fit the brightness profiles by projecting a spherically symmetric double β-model,

$$n_e(r) = \frac{n_0}{1+f}\left[\left(1+\frac{r^2}{r_{c1}^2}\right)^{-\frac{3}{2}\beta_1} + f\left(1+\frac{r^2}{r_{c2}^2}\right)^{-\frac{3}{2}\beta_2}\right], \quad (3)$$

where n_0 (central density for the sum of the two components), r_{c1}, r_{c2}, β_1, β_2, and f were free parameters. We ignore the very mild temperature dependence of the X-ray emissivity in this *Chandra* band and the relevant range of temperatures. Fits to the brightness profile were done out to R_{500} or as far in radius as the *Chandra* coverage allowed, which in all cases was far beyond the cores. While such a model is not physically motivated (and no physical significance should be assigned to the particular values of r_c and β), it fits all our clusters well, which is what we need for determining the central entropy. For those clusters where a single β-model provided a good fit, we set $f = 0$. Example cool-core fits with single and double β-models are shown in Figure 1, and fit results for all clusters are given in Table 4. We do not derive errors on best-fit quantities, because statistical errors are negligible and uncertainties of the geometry dominate. The uncertainties on entropy (Table 5) will be dominated by the temperature accuracy.

5.3. Spectral Analysis

We derived the temperatures of the intracluster medium using the *Chandra* data as follows. For each observation, we extracted a spectrum of the cluster for each region of interest, and generated the instrument responses (ARF and RMF) using the current calibration files (version N0008 for the telescope effective area, N0006 for the CCD quantum efficiency, and N0009 for the ACIS time-dependent low-energy contamination model).

The background spectra were extracted for the same regions from the corresponding blank-sky data sets, normalized as in Section 5.1. To ensure that the sky-variable soft cosmic X-ray background is subtracted correctly, we checked for the presence of a significant excess/deficit of soft X-ray thermal emission in the spectrum using local background regions. In those cases where significant systematic residuals were found, they were modeled with a low-temperature APEC (Astrophysical Plasma Emission Code) or absorbed power law and then included as a fixed additional background component in the spectral fits, normalized by the area of the region, as in Vikhlinin et al. (2005). This has little effect in the cores, but affects the fits in the outskirts.

The cluster X-ray emission was modeled with an absorbed, single-temperature APEC model in the the 0.7–7 keV energy band, with the metal abundance free to vary. For the full-cluster spectra, the column density of absorption N_H was allowed to vary. If the best-fit N_H value was consistent with that from the

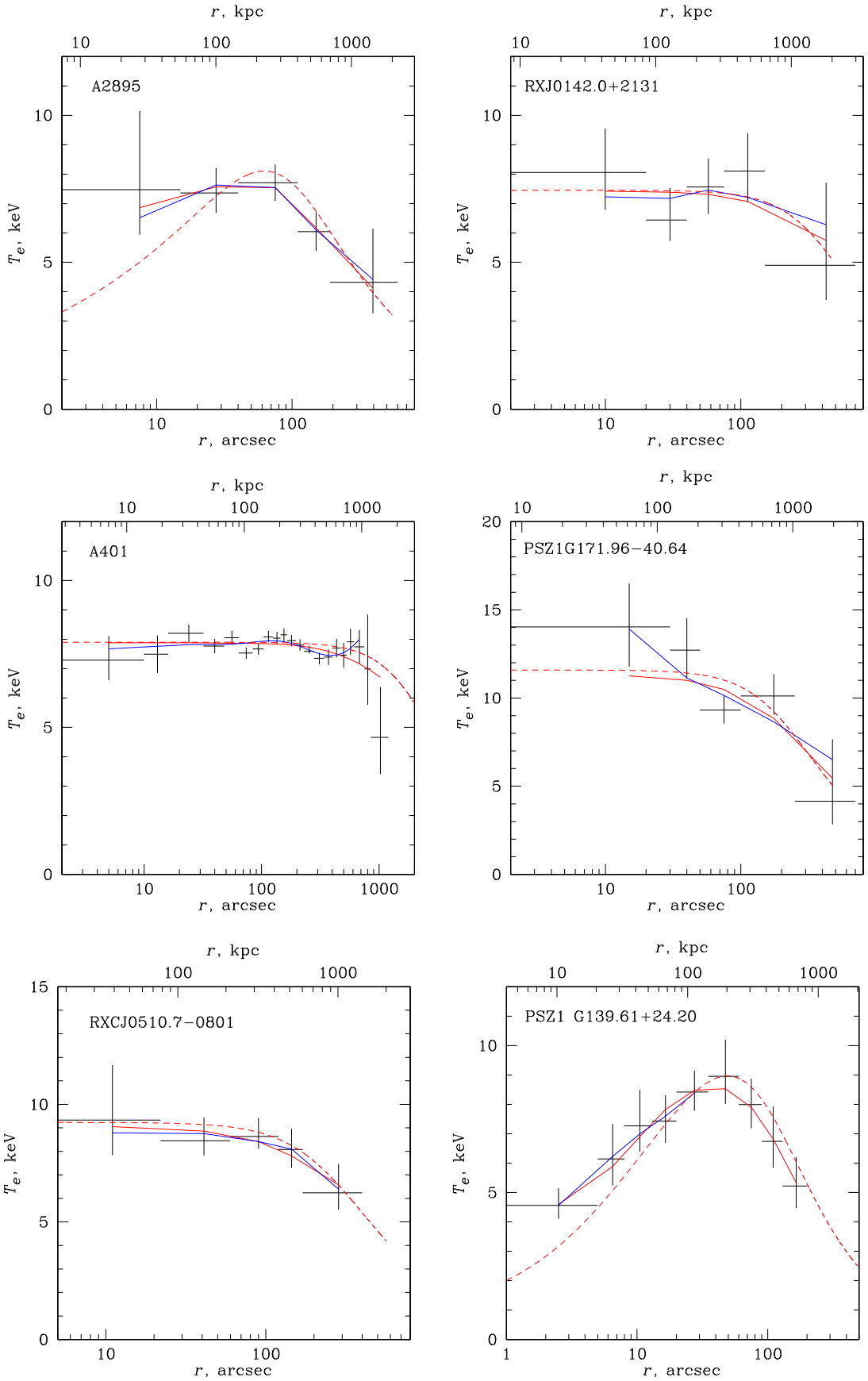

Figure 2. Temperature profiles for A2895, RXC J0142.0+2131, A401, PSZ1G171.96−40.64, RXC J0510.7−0801, and PSZ1G139.61+24.20. Crosses are the observed projected temperatures. Solid and dashed red lines show the best-fit three-dimensional model and the corresponding projected profile, respectively, and solid blue lines show the best-fit entropy model (Section 5.5 and Table 5).

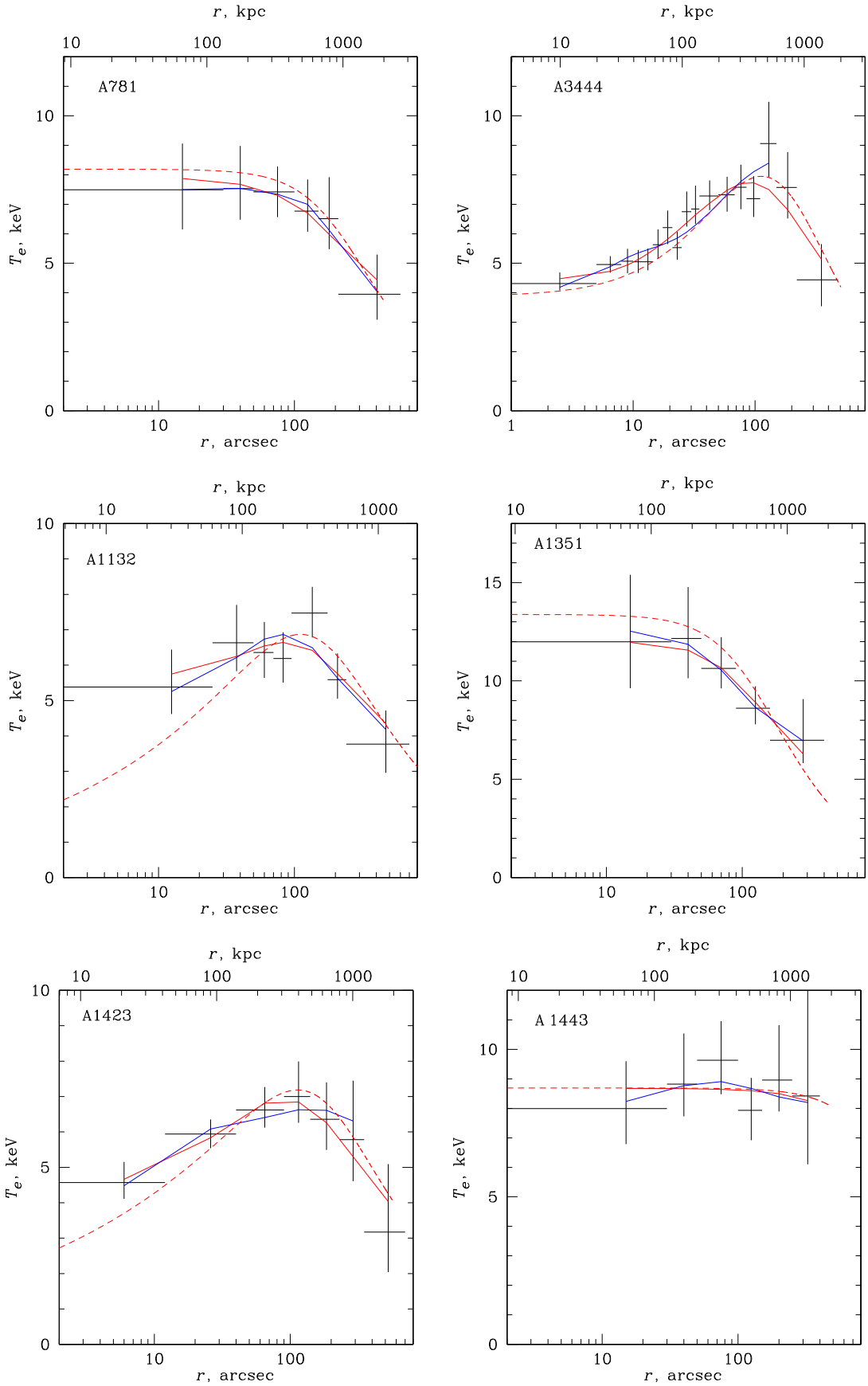

Figure 3. Same as Figure 2, but for A781, A3444, A1132, A1351, A1423, and A1443.

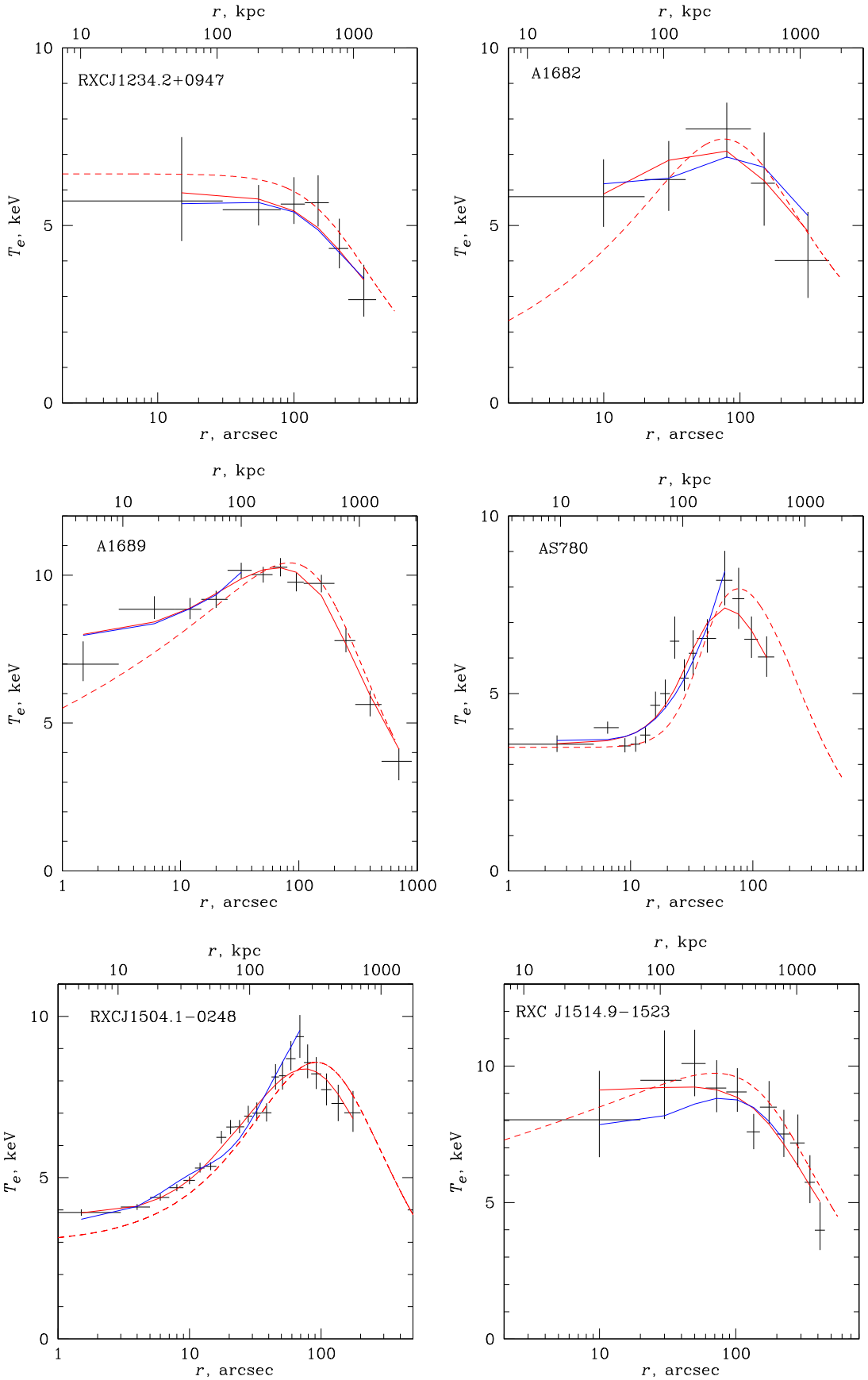

Figure 4. Same as Figure 2, but for RXC J1234.2+0947, A1682, A1689, AS 780, RXC J1504.1−0248, and RXC J1514.9−1523.

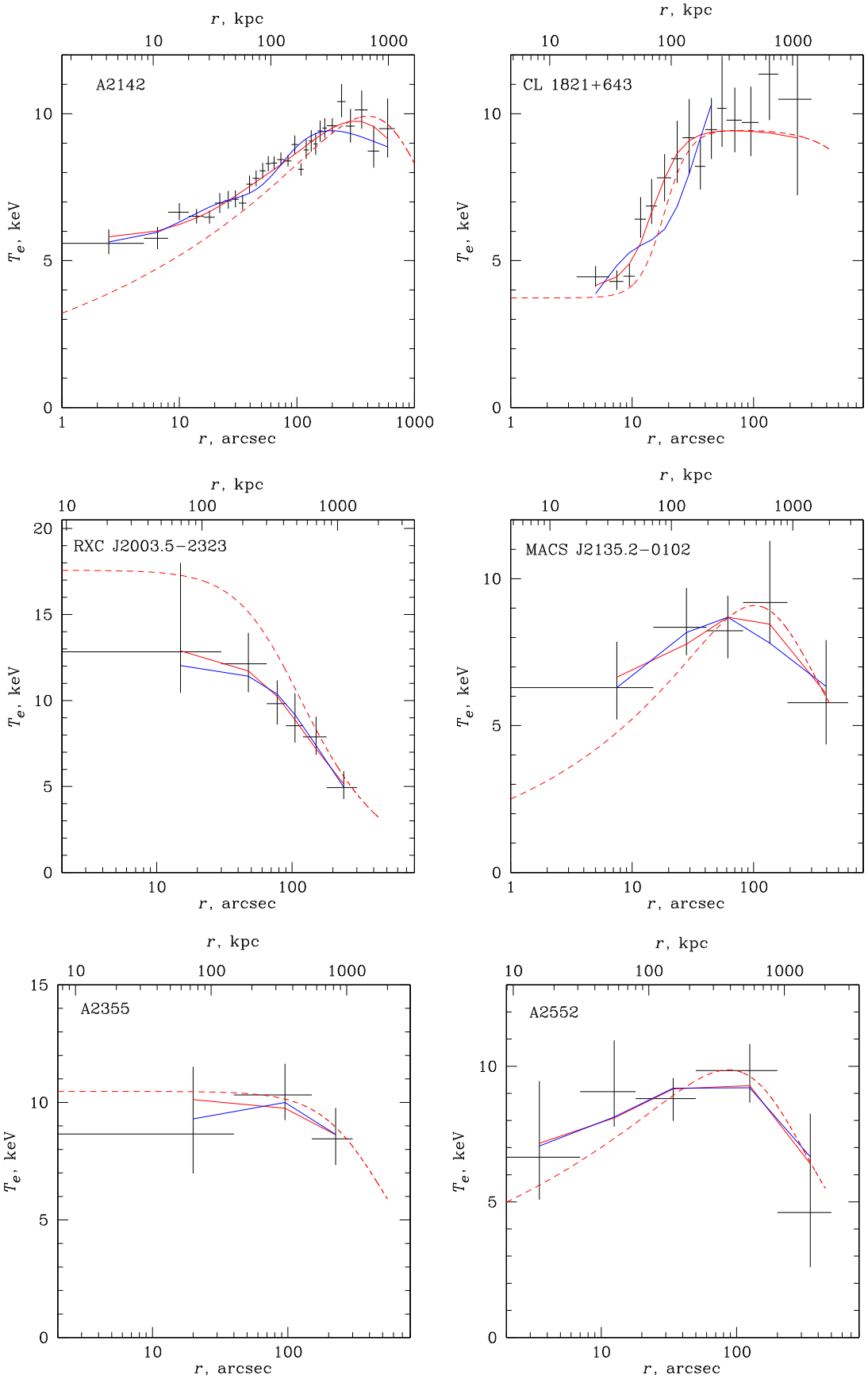

Figure 5. Same as Figure 2, but for A2142, CL 1821+643, RXC J2003.5−2323, MACS J2135.2−0102, A2355, and A2552.

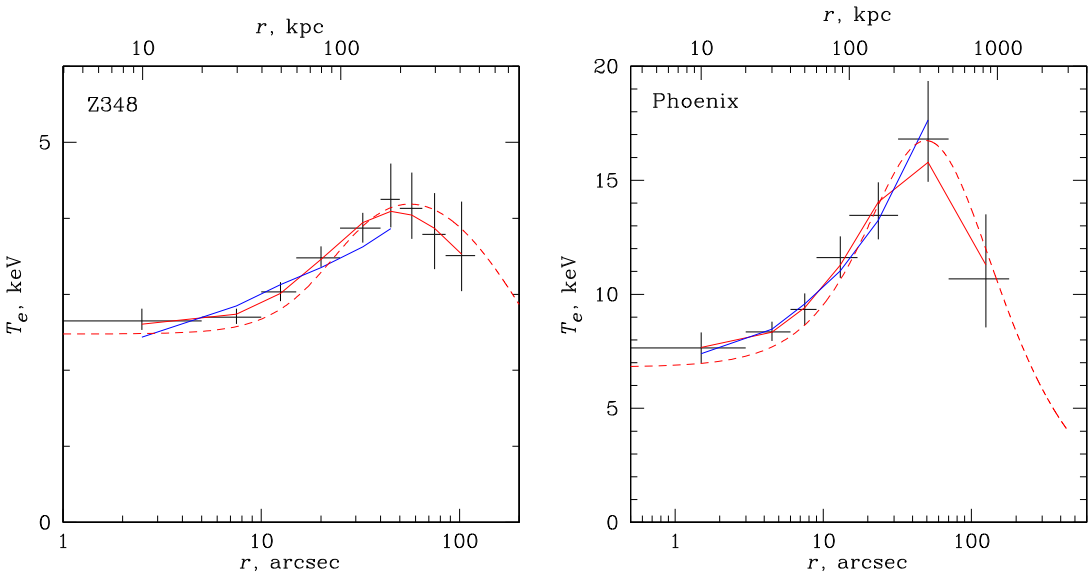

Figure 6. Same as Figure 2, but for Z348 and the Phoenix cluster.

Leiden/Argentine/Bonn radio survey of Galactic H I (Kalberla et al. 2005), we fixed it at the database value for subsequent analysis. The adopted $N_{\rm H}$ values are listed in Table 3.

For several clusters, we combined multiple *Chandra* observations (Table 3) by fitting their spectra simultaneously with the temperature and metal abundance of the hot APEC components tied together. For RXC J1504.1–0248, for which the observations had the same pointing position and roll angle and thus had the same responses, we instead coadded the spectra.

5.4. Average Cluster Temperatures

One of the quantities that we correlate with the presence of a radio halo is the global cluster temperature. In addition, for those clusters in the supplementary sample that do not have *Planck* masses, we estimate total masses from the M_{500}–$T_{\rm X}$ relation (Section 4). For 29 clusters in the statistical sample and for most in the supplementary one, we used core-excised global temperatures from C08. For the remaining clusters in the supplementary sample and for 12 in the statistical one with significantly better recent *Chandra* observations, we derived global temperatures (Section 5.3) using a spectrum extracted from an annulus with $70\,{\rm kpc} < r < R_{2500}$[8] as in C08. The core-excised temperatures, $T_{\rm X,ce}$, of all clusters are summarized in Tables 6 and 7. The exceptions are 2A 0335+096, Perseus, and Ophiuchus, for which we used average temperatures from *ASCA*[9] because of *Chandra*'s limited radial coverage. Another nearby cluster for which we used the total temperature from the literature is A193, a clear non-cool-core cluster, for which core excision would not change the temperature significantly. For cool cores, this should result in slightly underestimated masses from the M_{500}–$T_{\rm X}$ relation. This will not affect our qualitative conclusions.

[8] R_{2500} is the radius that encloses a mean overdensity of 2500 with respect to the critical density at the cluster redshift.

[9] *Advanced Satellite for Cosmology and Astrophysics.*

5.5. Temperature and Specific Entropy Profiles

We obtained radial temperature profiles by fitting spectra in annuli centered on the peak of the X-ray surface brightness, or on the centroid for disturbed clusters without a well-defined peak. The radial bins were selected as a compromise between the need to sample well the decline in temperature in the cores and to keep the uncertainties small. The maximum radius was as far as the detector coverage and the background uncertainties allowed; this is unimportant because we are interested in the cores. The spectra were fit as described in Section 5.4, with metallicities allowed to vary at small radii (since we expect strong gradients in cool cores) and fixed at 0.2 solar at large radii. $N_{\rm H}$ was fixed at the full-cluster values given in Table 3. The resulting projected temperature profiles for the clusters analyzed in this work are shown in Figures 2–6, except for A1733, which has only a 7 ks *Chandra* exposure (see below).

Our goal here is to derive the specific entropy floor in cluster centers, defined in the same way as in C09 (Section 4). For this purpose, we take our best-fit 3D density profile in the form of Equation (3), assume the radial dependence of entropy given by Equation (2), and calculate a temperature at a given radius from Equation (1). These temperature values are then averaged within each radial bin of the measured temperature profiles using the weighting of Mazzotta et al. (2004). The average values are compared with the observed temperature profiles, and the parameters K_0, K_{100}, and α are fit in such a way. Because of the limited modeling freedom of Equation (2), such a temperature profile usually described the cool cores well but often not the regions outside the core. Therefore, we only used the radii where the profile fit well, similarly to C09. The modeled projected temperature profiles are shown as blue lines overlaid on the measured profiles in Figures 2–6, and the best-fit entropy profile parameters, as well as the maximum radius used for the fit, are given in Table 5. For A1733, the central entropy is estimated using the best-fit density profile and the temperature within the central $r = 120\,{\rm kpc}$ region, which is enough to determine that it is not a cool core (Table 6).

For reference in our future work, and to verify the above model, we also fit the observed temperature profiles with a

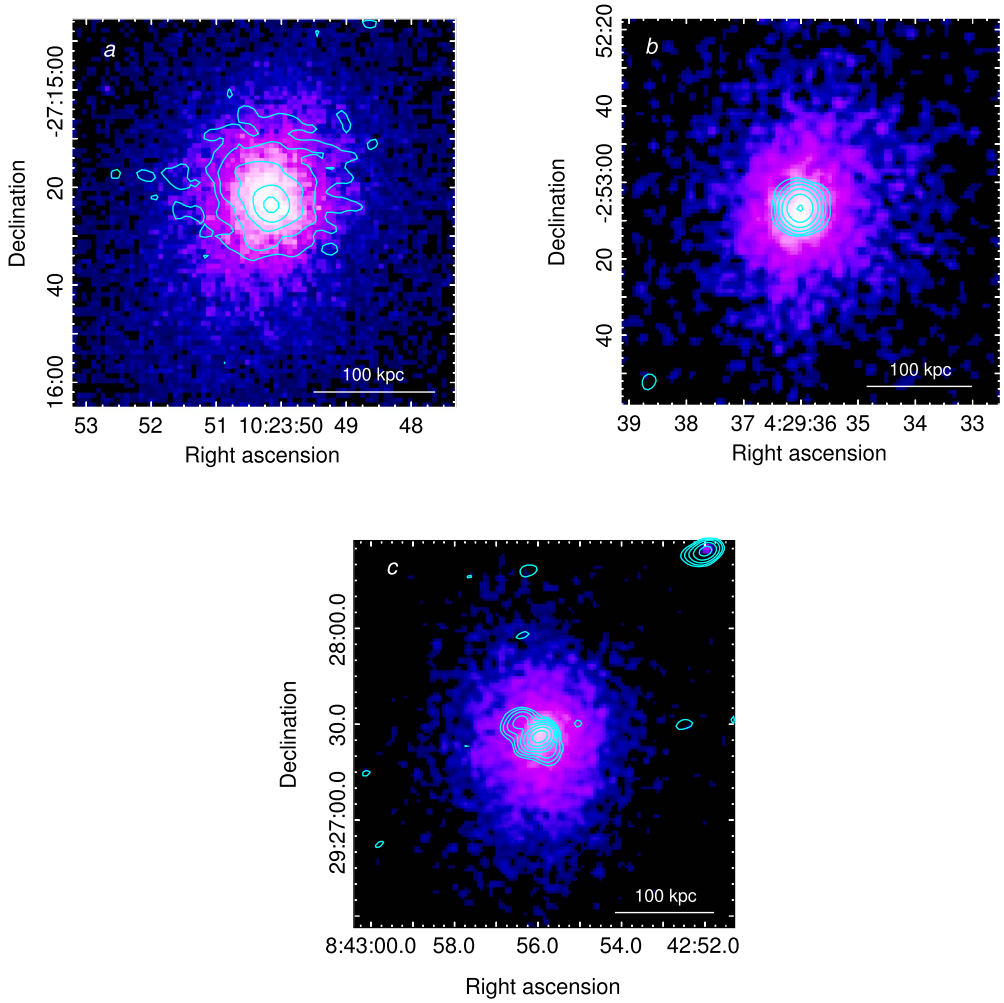

Figure 7. (a) Radio minihalo in the cool core of A3444, overlaid on the *Chandra* 0.5–4 keV image. The radio contours are from a VLA BnA-configuration image at 1.4 GHz (from G17). The restoring beam is 5″ and rms noise is 35 μJy beam^{-1}. Contours are 0.09, 0.18, 0.36, 0.72, 1.44 mJy beam^{-1}. (b), (c) Examples of two cool-core clusters, MACS J0429.6−0253 and MS 0839.8+2938, without a minihalo. For both clusters, the VLA B-configuration images at 1.4 GHz are overlaid as contours on the *Chandra* 0.5–4 keV image. For MACS J0429.6-0253, the restoring beam is 5″ × 4″ and rms noise is 40 μJy beam^{-1}. Contours are 0.1, 0.4, 1.6, 6.4, 25.6, 104.4 mJy beam^{-1}. For MS 0839.8+2938, the restoring beam is 6″ × 4″ and rms noise is 40 μJy beam^{-1}. Contours start at $+3\sigma$ and then scale by a factor of 2.

more complex phenomenological 3D temperature model used by Vikhlinin et al. (2006):

$$T(r) = T_0\ t_{\rm cool}(r)\ t(r), \tag{4}$$

where

$$t(r) = \left(\frac{r}{r_t}\right)^{-\alpha}\left[1 + \left(\frac{r}{r_t}\right)^{b}\right]^{-c/b} \tag{5}$$

describes the temperature profile outside the central cooling region and

$$t_{\rm cool}(r) = \frac{x + T_{\rm min}/T_0}{x + 1},\ \ x \equiv \left(\frac{r}{r_{\rm cool}}\right)^{a_{\rm cool}} \tag{6}$$

describes the temperature decline in the central region. T_0, r_t, α, b, c, $r_{\rm cool}$, $a_{\rm cool}$, and $T_{\rm min}$ are free parameters. The term $t_{\rm cool}(r)$ was required only in several cases with a strong radial increase of the temperature profile in the core; in most cases, setting $t_{\rm cool}(r) \equiv 1$ was sufficient for a good fit, because the term $t(r)$ alone can describe a temperature dip in the center. We also fixed $b = 2$ and $c = 1$, which provides a good fit in all cases. The model was projected along the line of sight and within each radial bin and fit to the observed projected temperature profiles. The best-fit profile parameters are given in Table 5. The 3D and the corresponding projected profiles are shown by red curves (dashed and solid, respectively) in Figures 2–6. Because this model is more flexible, it can describe the whole radial range of the measured temperatures. Comparison with the profiles for the entropy model (blue lines) shows that the entropy model provides an adequate fit to the temperature in the cores of all clusters.

Because we will combine the central entropy values from C09 and from our new analysis, we checked their consistency using RXC J1504.1–0248, one of the clusters in the C09 sample for which we used a more recent *Chandra* data set. Our best-fit central density (from a double β-model fit, see Figure 1) is only 7% higher than that in C09 (who derived it using the deprojection method), and our value for the entropy floor of $K_0 = 11.1 \pm 0.3$ keV cm^2 is consistent with, and more accurate than, the C09 value of $K_0 = 13 \pm 1$ keV cm^2. Other parameters of the core entropy profile are in agreement as well. The accuracy of K_0 depends on the number of temperature bins in the core, which is where the new data helped.

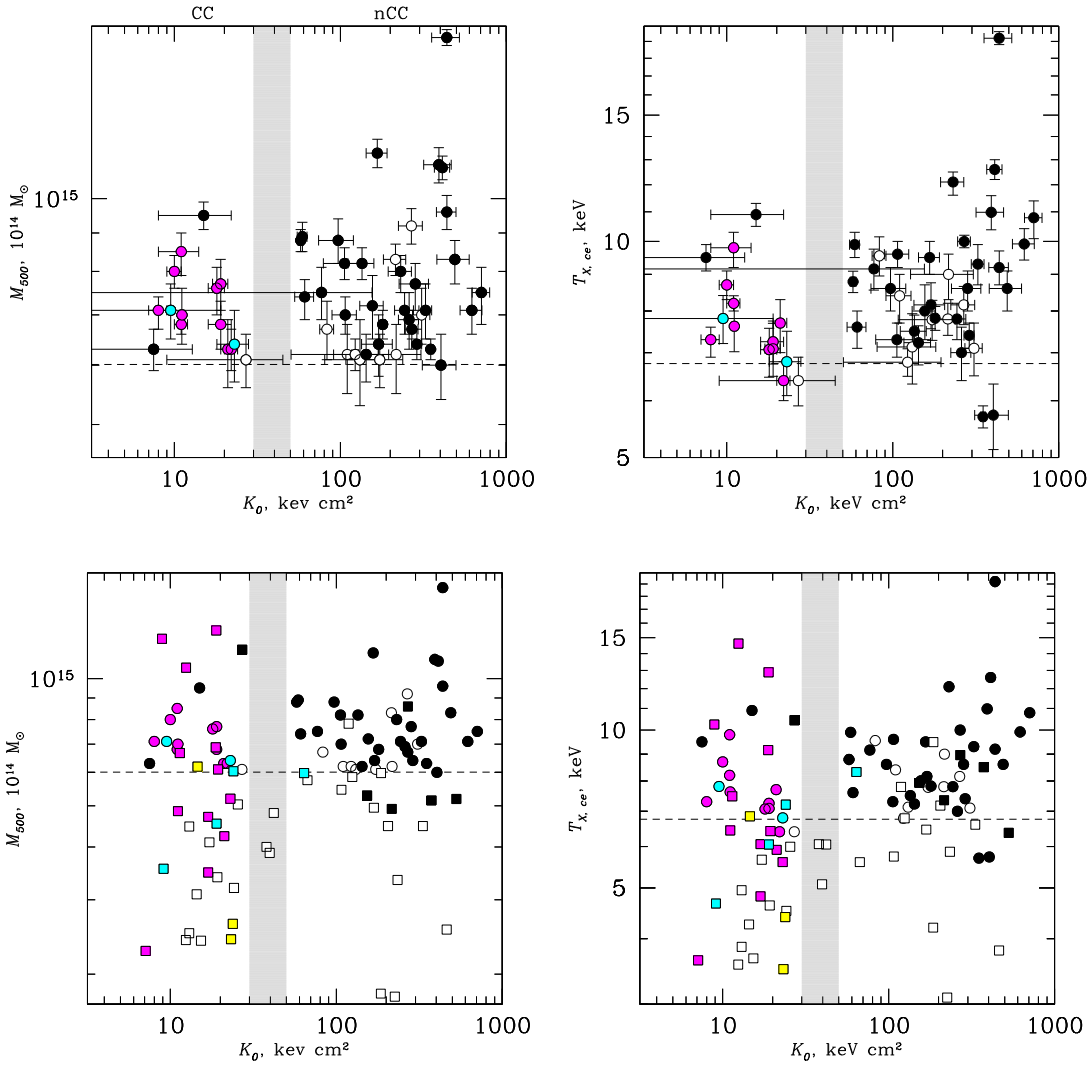

Figure 8. Upper panels: plots of M_{500}–K_0 and $T_{X,cc}$–K_0 for the *Chandra* clusters in our statistical sample. Clusters with minihalos are shown as magenta (confirmed detections) and cyan (candidates), radio-halo clusters (including candidates) are shown in black, and empty circles are clusters with no detected central diffuse radio emission. Clusters without high-sensitivity radio observations (RXC J0510.7−0801, RXC J0520.7−1328, MACS J2135.2−0102, A2355, and A1733) are not included in the plots (they all have $K_0 > 80$ keV cm^2; Table 6). Lower panels: the same for the combined statistical sample (circles) and supplementary sample (squares). Error bars are omitted for clarity. Symbol colors are the same. Yellow shows clusters hosting a central diffuse radio source whose classification as a minihalo is uncertain (ZwCl 1742.1+3306, MACS J1931.8–2634, A2626; Section 3.2). The combined sample extends to lower masses, where minihalos appear to be less frequent.

6. Radio Analysis

We analyzed VLA archival observations at 1.4 GHz of those clusters in our supplementary sample with no high-sensitivity and multi-resolution radio images on the angular scales of minihalos in the literature (nine clusters). The observations were chosen to be suitable to search for diffuse radio emission on the scale of the cluster core, i.e., deep and with a good sampling of the *uv* plane, particularly at short spacings, which are crucial to properly image extended radio emission of low surface brightness. Furthermore, we selected observations with a range of angular resolutions that allow us to discriminate between genuine diffuse emission and a blend of individual radio galaxies, as well as to separate a possible minihalo from the radio source associated with the cluster central galaxy.

Here we provide a brief description of the data reduction. The observation details, radio images, and notes on the individual clusters are presented in Appendix A. The data were calibrated and reduced in the standard fashion using the NRAO Astronomical Image Processing System (AIPS) package. Self-calibration was applied to reduce the effects of residual phase and amplitude errors in the data and improve the quality of the final images. For each cluster, the observations in different array configurations were processed and imaged separately. When possible, data from different dates and configurations were combined together in the *uv* or image plane. Sets of images were produced with different weighting schemes, ranging from pure uniform weighting (Briggs "robustness" parameter (Briggs 1995) $ROBUST = -5$) to natural weighting ($ROBUST = +5$), to enhance any possible extended emission. The flux density scale was set using the coefficients of Perley & Butler (2013), and residual amplitude errors are within 3%–5%.

No new minihalos were detected among the nine clusters analyzed here. As an illustrative example, in Figure 7 we show a comparison between a known minihalo (in our statistical sample)

Table 8
Newly Analyzed 1.4 GHz VLA Observations

Cluster Name	Configuration	Project	Date	Time (minutes)
A193	C	AM735	2002 Nov 30	118
	C	AM702	2002 Oct 28	37
	D	AM702	2001 Oct 15	55
A383	A	AR369	1996 Nov 17	54
	A	AR369	1996 Nov 19	100
	C	AM072	2002 Oct 28	61
	D	AM072	2001 Oct 21	60
MS 0440.5+0204	A	AI0072	1998 Apr 19, 20	360
	C	AS0873	2006 Dec 14	43
MACS J0429.6−0253	A	AT0318	2006 Apr 03	52
	B	AT0318	2006 Sep 06	35
MS 0839.8+2938	B	AH0190	1985 Apr 25	30
	C	AH0491	1993 Jun 26	58
A1204	C	AJ0242	1994 Dec 05	74
A2125	C	AD0311	1993 Jul 29	343
A2420	CnB	AM0702	2002 Sep 24, 29	60
	DnC	AM0702	2001 Oct 6, 7	60
A2556	CnB	AM0702	2002 Sep 29	60
	DnC	AM0702	2001 Oct 07	60

Note. Column 1: cluster name. Column 2: VLA configuration. Columns 3 and 4: project code and observation date. Column 5: total time on source.

Table 9
Properties of the VLA Radio Images

Cluster Name	Configuration	FWHM, p.a. ($'' \times ''$, deg)	rms (μJy beam^{-1})	$S_{1.4\,\mathrm{GHz}}$ (mJy)	LDS (Mpc)
A193	C	16 × 14, 15	40	60 ± 3	0.8[a]
	C+D	25 × 19, −4	35	61 ± 3	0.8
A383	A	1.5 × 1.3, −10	40	41 ± 2	0.12
	C+D	23 × 18, 8	45	41 ± 2	2.8
MS 0440.5+0204	A	1.5 × 1.3, −48	30	43.6 ± 2.2[b]	0.12
	C	15 × 13, −13	65	43 ± 2	2.8[a]
MACS J0429.6-0253	A	1.8 × 1.3, −15	38	133 ± 7	0.2
	B	5 × 4, −2	40	138 ± 7	0.6
MS 0839.8+2938	B	6 × 4, −65	40	25 ± 1	0.4
	C	14 × 13, 12	53	26 ± 1	2.9[a]
A1204	C	15 × 13, −3	28	1.8 ± 0.1	2.6[a]
A2125	C	14 × 14, −3	58	19 ± 1	3.5[a]
A2420	CnB	14 × 6, 0	50	198 ± 10	1.4[a]
	DnC	50 × 20, 0	65	197 ± 10	1.4
A2556	CnB	14 × 8, 71	45	20 ± 1[c]	1.5[a]
	DnC	47 × 25, 77	60	22 ± 1	1.5
	CnB+DnC	17 × 12, 60	35	22 ± 1[c]	1.5

Notes. Column 1: cluster name. Column 2: VLA configuration. Columns 3: FWHM and position angle (p.a.) of the radio beam. Column 4: image rms level (1σ) for *ROBUST* = 0 in IMAGR. Column 5: total flux density of the central radio emission. Column 6: largest linear structure detectable by the observation (LDS), as derived from the maximum angular scale that can be imaged reasonably well by VLA long-synthesis observations.
[a] Although the shortest baseline is the same as in D configuration, the surface brightness sensitivity to extended structure is significantly less than that of the D configuration, but still high enough to detect diffuse emission on the core scale at the typical brightness of minihalos (Appendix B).
[b] Sum of the flux densities of the double source (33.0 ± 1.7 mJy) and head–tail radio galaxy (10.6 ± 0.5 mJy).
[c] Sum of the flux densities of the central radio galaxy (1.8 ± 0.1 mJy in the CnB image and 1.9 ± 0.1 mJy in the CnB+DnC image) and head–tail radio galaxy (18 ± 1 mJy and 20 ± 1 mJy).

and two nondetections based on our radio analysis. Panel (a) shows the minihalo in the cool-core cluster A3444 (from G17; see also Venturi et al. 2008; Kale et al. 2015). Panels (b) and (c) show radio/X-ray overlays for MACS J0429.6-0253 and MS 0839.8+2938, both cool cores in our supplementary sample. All three radio images have similar angular resolution ($\sim 5''$) and sensitivity ($1\sigma \sim 35$–$40\,\mu$Jy beam^{-1}). The observations also have similar sampling of short spacings in the *uv* plane, which ensures the possibility of detecting extended emission on a largest scale of $\sim 2'$. This corresponds to a physical scale of $\sim$470 kpc for A3444, $\sim$640 kpc for MACS J0429.6-0253, and $\sim$390 kpc for MS 0839.8+2938, and thus is well beyond the region occupied by the central radio galaxy. While a minihalo is clearly well detected in A3444, no indication of diffuse radio

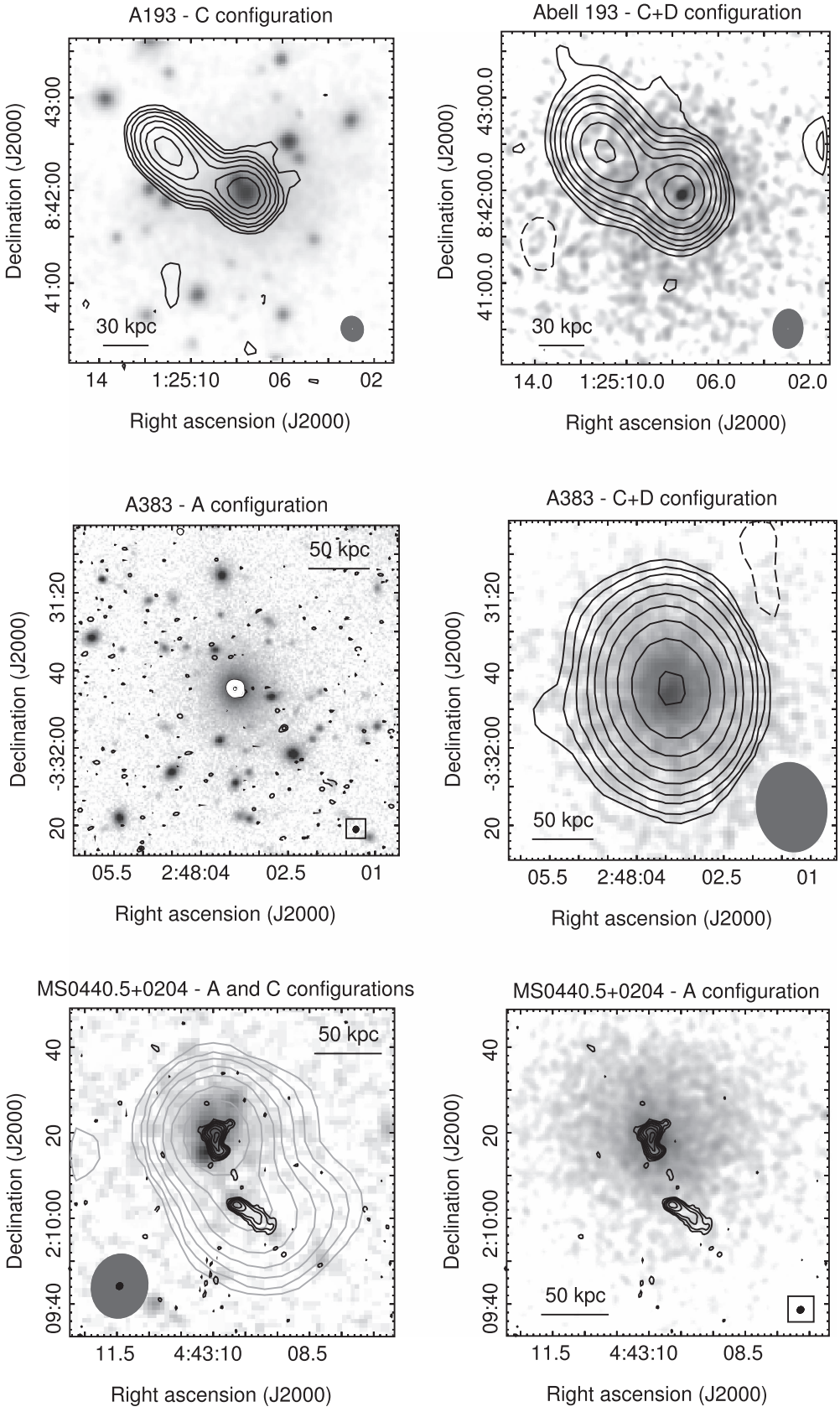

Figure 9. Upper and middle panels: VLA 1.4 GHz combined radio images of A193 and A383, overlaid on the optical *r*-band SDSS images (left) and smoothed X-ray *Chandra* images in the 0.5–4 keV band (right). Contours start at $+3\sigma$ and then scale by a factor of 2. When present, contours at -3σ are shown as dashed. Restoring beams (also shown as ellipses in the lower corner of each image) and rms noise values are as listed in Table 9. Bottom panels: VLA C-configuration (gray contours) and A-configuration (black contours) images of MS 0440.5+020, overlaid on the POSS-2 red optical image (left). On the right, the A-configuration image is overlaid on the smoothed X-ray *Chandra* image in the 0.5–4 keV band. Contours start from $+3\sigma$ and then scale by a factor of 2. No levels at -3σ are present in the portion of the images shown. Restoring beams (also shown as ellipses in the lower right corner of each image) and rms noise values are as listed in Table 9.

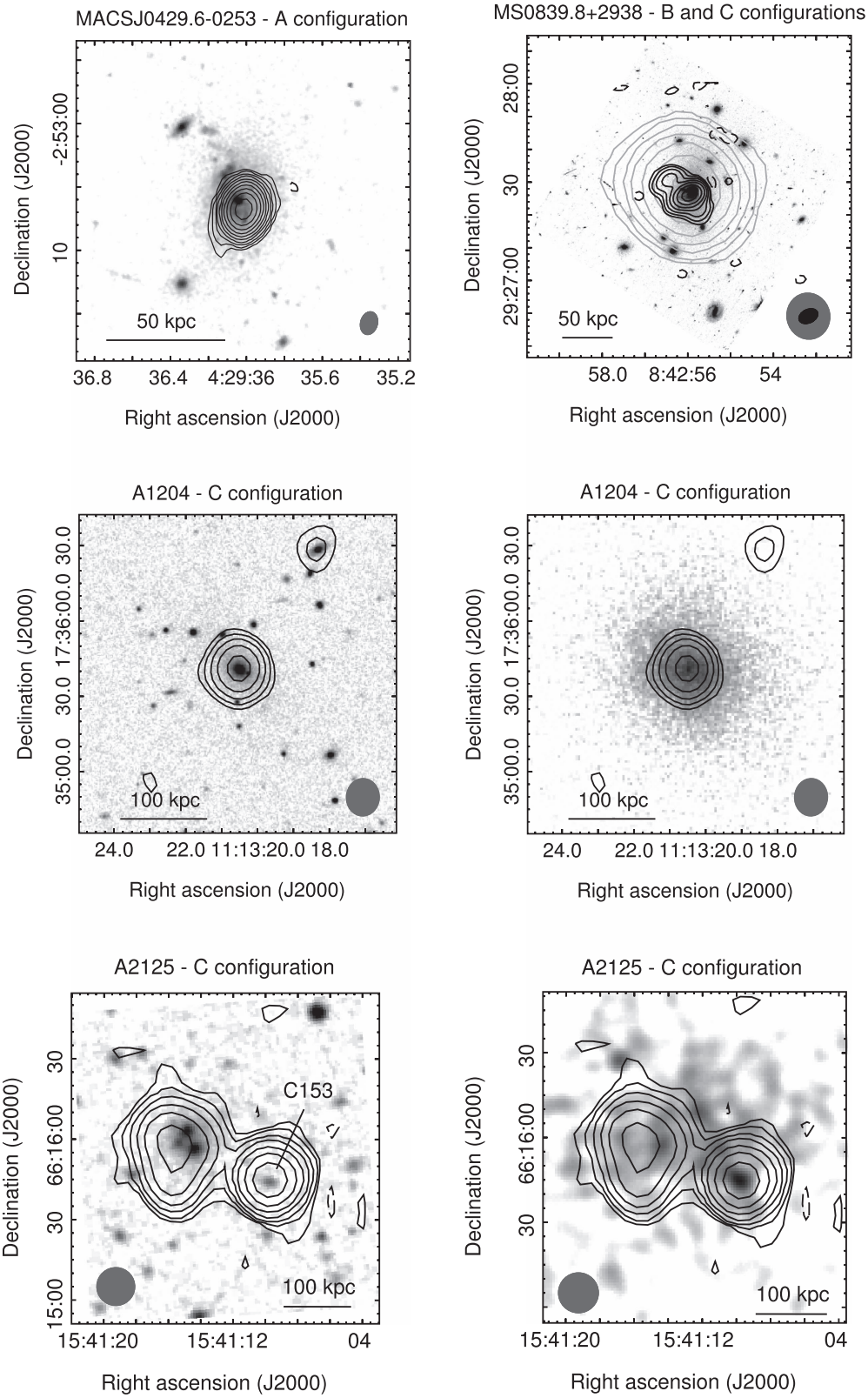

Figure 10. Upper panels: VLA 1.4 GHz radio images of MACS J0429.6–0253 (left) and MS 0839.8+2938 (right), overlaid on the preview *HST* WFPC2 images (programs 11103 and 11312). Middle panels: VLA 1.4 GHz radio image of A1204, overlaid on the optical *r*-band SDSS image (left) and smoothed X-ray *Chandra* image in the 0.5–4 keV band (right). Bottom panels: VLA 1.4 GHz radio image of A2125, overlaid on the optical POSS-2 red optical images (left) and smoothed X-ray *Chandra* images in the 0.5–4 keV band (right). In all panels, contours start at $+3\sigma$ and then scale by a factor of 2. When present, contours at -3σ are shown as dashed. Restoring beams (also shown as ellipses in the lower corner of each image) and rms noise values are as listed in Table 9.

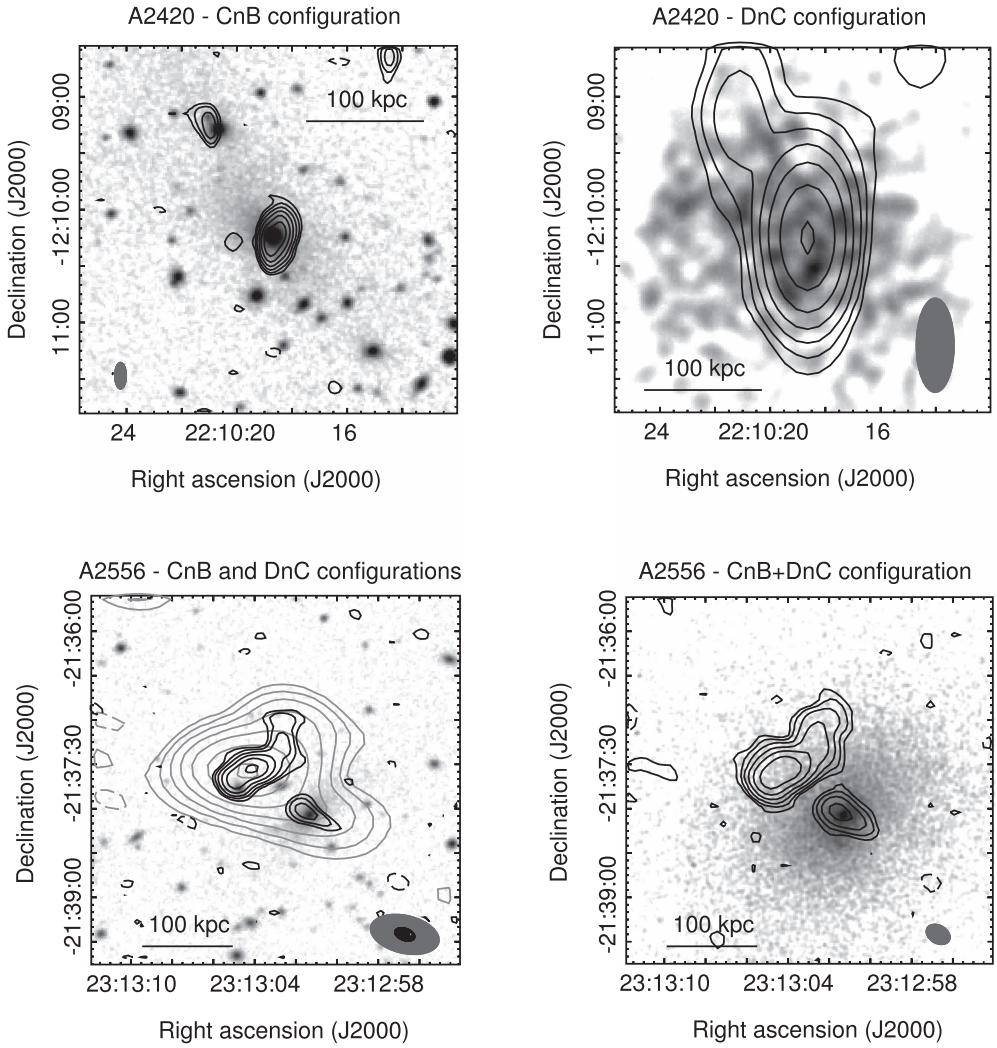

Figure 11. VLA 1.4 GHz radio images of A2420 (upper panels) and A2556 (bottom panels), overlaid on the optical POSS-2 red optical images (left) and smoothed X-ray *Chandra* images in the 0.5–4 keV band (right). In all panels, contours start at $+3\sigma$ and then scale by a factor of 2. When present, contours at -3σ are shown as dashed. Restoring beams (also shown as ellipses in the lower right corner of each image) and rms noise values are as listed in Table 9.

emission is visible in the cores of the other clusters at a similar sensitivity level.

7. Discussion

The purpose of this study is to quantify how frequently radio minihalos occur in clusters. The top panels in Figure 8 plot the clusters in our mass-limited sample in the planes M_{500}–K_0 and $T_{\rm X,cc}$–K_0 (in the latter panel, the approximate temperature from the M_{500}–$T_{\rm X}$ relation that corresponds to our mass cut is shown by a dashed line). As noted by C09, Rossetti et al. (2013), and others, the cluster sample clearly separates into two populations: cool cores with $K_0 \lesssim 30$ keV cm^2 and non-cool cores (most of which are obvious mergers) with $K_0 \gtrsim 50$ keV cm^2. The fraction of cool cores in our *Planck*-selected sample is 26% (15 out of 58), similar to the fraction found in a much larger *Planck*-selected sample (Andrade-Santos et al. 2017) and lower than that seen in X-ray-selected samples of nearby clusters (e.g., Rossetti et al. 2016).

As shown before (e.g., Cassano et al. 2013; Rossetti et al. 2013; Cuciti et al. 2015; Yuan et al. 2015), giant halos (black symbols) are found almost exclusively in non-cool-core clusters. We find that minihalos (magenta symbols) are indeed found exclusively in cool cores, confirming previous non-statistical findings (e.g., Giacintucci et al. 2014b; Kale et al. 2015; Yuan et al. 2015). A new result that is evident in Figure 8 (top panels) is that *almost all* cool cores in a complete sample of massive clusters—12 out of 15, or 80%—possess a minihalo. Radio minihalos are not that rare after all.

It is interesting to extend the mass range of the sample toward lower masses and temperatures. According to Cuciti et al. (2015), the probability of finding a giant radio halo in merging clusters increases with the total mass. This is instructive for the origin of giant halos, because it implies a statistical link between the mechanical energy available during mergers and the generation of these sources (e.g., Cassano et al. 2006, 2016). It is interesting to check whether minihalos exhibit a similar behavior. The lower panels in Figure 8 show our combined statistical + supplementary sample, which includes all the known 22 confirmed minihalos (magenta points) and six candidates (cyan points). This combined sample extends a factor of 3 below the mass cut of the statistical one, and also adds a number of massive systems. We do see the lower frequency of the giant radio halos in cooler clusters, observed in Cassano et al. (2013) and Cuciti et al. (2015). Similarly, at lower masses, a large fraction of cool cores

Table 10
Properties of the Radio Images and Central Diffuse Radio Sources

Cluster Name	ν (GHz)	FWHM ($'' \times ''$)	rms (1σ) (mJy beam^{-1})	$\frac{\mathrm{LDS}}{2}$ (Mpc)	R_{radio} (Mpc)	$\frac{\langle \mathrm{SB_{radio}} \rangle}{1\sigma}$	References
Clusters with Minihalos in the Statistical Sample							
A478	1.4	30 × 30	0.05	0.7	0.16	7.9	4
RBS 797	1.4	19 × 12	0.04	2.2	0.12	12.2	2
A3444	0.6	7 × 7	0.04	2.0	0.12	10.4	3
A1835	1.4	51 × 45	0.04	1.8	0.24	23.7	2
AS 780	0.6	6 × 4	0.07	1.9	0.05	17.0	5
RXC J1504.1−0248	0.3	11 × 10	0.10	3.3	0.14	22.7	6
A2029	1.4	57 × 45	0.04	0.6	0.25	10.8	2
A2204	1.4	6 × 5	0.03	0.16	0.05	7.1	4
RXC J1720.1+2638	0.6	8 × 6	0.03	1.4	0.14	28.1	7
A2667	1.2	5 × 5	0.04	1.5	0.06	5.0	2
Clusters with Minihalos in the Supplementary Sample							
MACS J0159.8−0849	1.4	5 × 5	0.015	0.3	0.09	3.6	4
Perseus	0.3	51 × 77	1.4	0.9	0.13	98.7	8
MACS J0329.6−0214	1.3	5 × 5	0.03	1.2	0.07	6.3	2
2A 0335+096	1.4	30 × 27	0.04	0.3	0.07	10.2	2
A907	0.6	5 × 5	0.05	1.5	0.06	11.0	2
ZwCl 3146	0.6	9 × 7	0.09	2.2	0.08	6.1	5
RX J1347.5−1145	1.4	17 × 17	0.04	2.6	0.26	30.4	2
MS 1455.0+2232	0.6	6 × 5	0.07	2.0	0.12	4.1	9
RX J1532.9+3021	1.4	3 × 3	0.01	0.3	0.10	4.3	4
Ophiuchus	1.4	110 × 60	0.12	0.25	0.25	5.8	2
RXC J2129.6+0005	0.6	11 × 11	0.11	1.9	0.08	4.8	5
Phoenix	0.6	14 × 6	0.04	3.4	0.23	6.7	10
Clusters with Radio Halos in the Statistical Sample							
A2744	1.4	50 × 50	0.09	2.0	0.8	12.7	34
A209	1.4	60 × 40	0.05	1.5	0.5	9.3	12
A401	1.4	60 × 60	0.08	0.6	0.4	3.8	2
PSZ1 G171.96−40.64	1.4	50 × 50	0.12	1.9	0.6	4.5	13
A521	0.2	35 × 35	0.22	5.1	0.7	6.5	14
A520	1.4	26 × 26	0.03	1.5	0.5	4.2	15
A665	1.4	52 × 42	0.07	1.4	0.7	7.0	16
A697	0.3	47 × 41	0.15	4.1	0.6	9.6	17
A754	0.3	109 × 74	1.0	1.0	0.6	5.1	18
A773	1.4	30 × 30	0.03	1.6	0.5	4.7	34
A1300	0.3	28 × 28	0.50	4.3	0.5	4.2	11
A1351	1.4	20 × 18	0.05	2.1	0.5	3.2	19
A1443	0.3	27 × 27	0.36	3.9	0.6	1.8	20
A1689	1.4	67 × 52	0.10	1.3	0.7	5.0	2
A1758a	0.3	35 × 35	0.40	4.1	0.8	3.3	11
A1914	1.4	50 × 45	0.05	1.3	0.6	16.7	21
RXC J1514.9−1523	0.3	53 × 41	0.27	3.4	0.7	5.5	22
A2142	1.4	60 × 60	0.18	0.7	0.4	2.0	23
A2163	1.4	45 × 60	0.05	1.5	1.0	23.4	24
A2218	0.6	25 × 25	0.07	1.5	0.4	1.7	2
A2219	1.4	50 × 45	0.07	1.6	0.7	18.1	21
A2256	0.3	67 × 67	0.60	3.5	0.5	7.2	25
A2261	1.4	50 × 50	0.05	1.6	0.5	2.8	26
CL 1821+643	0.3	30 × 26	0.20	4.5	0.4	8.6	27
RXC J2003.5−2323	1.4	35 × 35	0.03	2.1	0.9	9.4	28
A2390	1.4	30 × 30	0.04	1.7	0.4	8.1	26
RXC J1314.4−2515	0.6	25 × 22	0.06	1.9	0.3	3.7	12
Clusters with Radio Halos in the Supplementary Sample							
A399	1.4	45 × 45	0.04	0.6	0.3	4.2	33
MACS J0417.5−1154	0.6	20 × 20	0.15	2.9	0.5	4.7	29

Table 10
(Continued)

Cluster Name	ν (GHz)	FWHM ($'' \times ''$)	rms (1σ) (mJy beam^{-1})	$\frac{\mathrm{LDS}}{2}$ (Mpc)	R_{radio} (Mpc)	$\frac{\langle \mathrm{SB_{radio}} \rangle}{1\sigma}$	References
A1995	1.4	30 × 30	0.05	2.1	0.3	4.4	30
A2034	1.4	44 × 40	0.04	0.9	0.3	7.0	30
A2255	0.3	54 × 64	0.10	3.7	0.8	15.7	31
A2319	1.4	119 × 110	0.40	0.9[a]	0.6	6.4	32

Note. Column 1: cluster name. Columns 2–4: frequency, beam FWHM, and rms noise (1σ, per beam) of the images used to measure the source radius. Images at 1.4 GHz are from VLA observations, all other frequencies are GMRT observations; for Perseus and A2255 we used WSRT images. Column 5: radius of the largest linear structure detectable by the observations, as derived from the maximum angular scale that can be imaged reasonably well by long-synthesis observations with the VLA, GMRT, and WSRT. Column 6: radius of the central diffuse radio source, defined as in Section 2, derived from the 3σ surface brightness isocontour. Column 7: ratio of the average surface brightness of the source ($\mathrm{SB_{radio}}$) and 1σ noise level of the image. Column 8: reference for the radio images. Reference code: (1) this work, (2) G17, (3) G17, (4) Giacintucci et al. (2014b), (5) Kale et al. (2015), (6) Giacintucci et al. (2011b), (7) Giacintucci et al. (2014a), (8) Sijbring (1993), (9) Venturi et al. (2008), (10) van Weeren et al. (2014), (11) Venturi et al. (2013), (12) Venturi et al. (2007), (13) Giacintucci et al. (2013), (14) Brunetti et al. (2008), (15) Vacca et al. (2014), (16) Giovannini & Feretti (2000), (17) Macario et al. (2010), (18) Macario et al. (2011), (19) Giacintucci et al. (2009a), (20) Bonafede et al. (2015), (21) Bacchi et al. (2003), (22) Giacintucci et al. (2011a), (23) Venturi et al. (2017), (24) Feretti et al. (2001), (25) Brentjens (2008), (26) Sommer et al. (2017), (27) Bonafede et al. (2014), (28) Giacintucci et al. (2009b), (29) Parekh et al. (2017), (30) Giovannini et al. (2009), (31) Pizzo & de Bruyn (2009), (32) Storm et al. (2015), (33) Murgia et al. (2010a), (34) Govoni et al. (2001).
[a] Combination of two VLA pointings offset by $12\farcm2$.

without minihalos (not detected at a similar radio sensitivity; see Section 5, Figure 7, and Appendix A) emerges, while almost all the additional *massive* cool cores do have minihalos, consistently with our finding for the statistical sample. Minihalos are still absent from the non-cool-core clusters (with the exception of the candidate minihalo in A1413); a few "warm cores" that appear in the gap $K_0 = 30$–50 keV cm^2 do not host minihalos (or giant halos) either. The apparent reduced frequency of minihalos at lower masses needs a proper statistical investigation that accounts for selection effects (e.g., what if the radio luminosity correlates with the cluster mass) and radio upper limits (for instance via injection of *fake* minihalos in the *uv* data, e.g., Kale et al. 2015), which will be the subject of future work.

8. Conclusions

The two new results of our study are: (a) almost all (12 out of 15, i.e., 80%) massive clusters with cool cores ($M_{500} > 6 \times 10^{14} M_\odot$ or $T \gtrsim 6$ keV) exhibit a radio minihalo, and (b) the fraction of minihalos appears to drop in cool cores with lower total cluster masses (or global temperatures). To make the former observation, we used a mass-limited cluster sample. For the latter result, we extended the sample to include more clusters with available *Chandra* and radio data, including higher-redshift and lower-mass clusters and all the other known minihalos (for a total of 28 minihalos, including six candidates).

These findings may encode information on the origin of minihalos. In the present study, we used only the presence or absence of a minihalo; we will investigate the correlation of the radio power with cluster mass, as well as with cool-core thermodynamic parameters, in the follow-up works. A few outliers may prove especially valuable, such as a minihalo in the low-mass cool core 2A 0335+096 (Sarazin et al. 1995), a giant halo in the high-mass cool core CL 1821+643 (Bonafede et al. 2014; Kale & Parekh 2016), a halo in A2390 (Sommer et al. 2017), whose cool core has a similar, unusually large radius (Vikhlinin et al. 2005), as well as the absence of minihalos from warm cores.

We thank the referee for their critical and helpful comments. S.G. acknowledges the support by the National Aeronautics and Space Administration, through *Chandra* Award Numbers G03-14140X, AR5-16013X, and G05-16136X. Basic research in radio astronomy at the Naval Research Laboratory is supported by 6.1 Base funding. R.C., T.V., and G.B. acknowledge partial support from PRIN INAF 2014. This research has made use of the NASA/IPAC Extragalactic Database (NED), which is operated by the Jet Propulsion Laboratory, California Institute of Technology, under contract with the National Aeronautics and Space Administration. The National Radio Astronomy Observatory is a facility of the National Science Foundation operated under cooperative agreement by Associated Universities, Inc.

Appendix A
Radio Observations and Images

Table 8 lists the VLA archival observations at 1.4 GHz reanalyzed in this work, as described in Section 6. Our final radio images are presented and compared to the cluster optical images (from SDSS,[10] POSS-2,[11] or *HST* WFPC2[12]) and X-ray *Chandra* images in Figures 9–11. The radio images of MACS J0429.6-0253 and MS 0839.8+2938 are overlaid on the *Chandra* images in Figure 7 and on the optical *HST* images in Figure 10 (upper panels). The image properties are summarized in Table 9. All the images shown here have been obtained with the *ROBUST* parameter set to 0 in the AIPS task IMAGR. The flux density of the unresolved radio galaxies was measured by fitting the sources with a Gaussian model (task JMFIT). For extended radio galaxies, the total flux density was determined using the task TVSTAT. All fluxes were measured on images corrected for the attenuation of the primary beam. A brief description of the radio emission in each individual cluster is given below.

[10] Sloan Digital Sky Survey.
[11] Second Palomar Observatory Sky Survey.
[12] *Hubble Space Telescope* Wide-Field Planetary Camera 2.

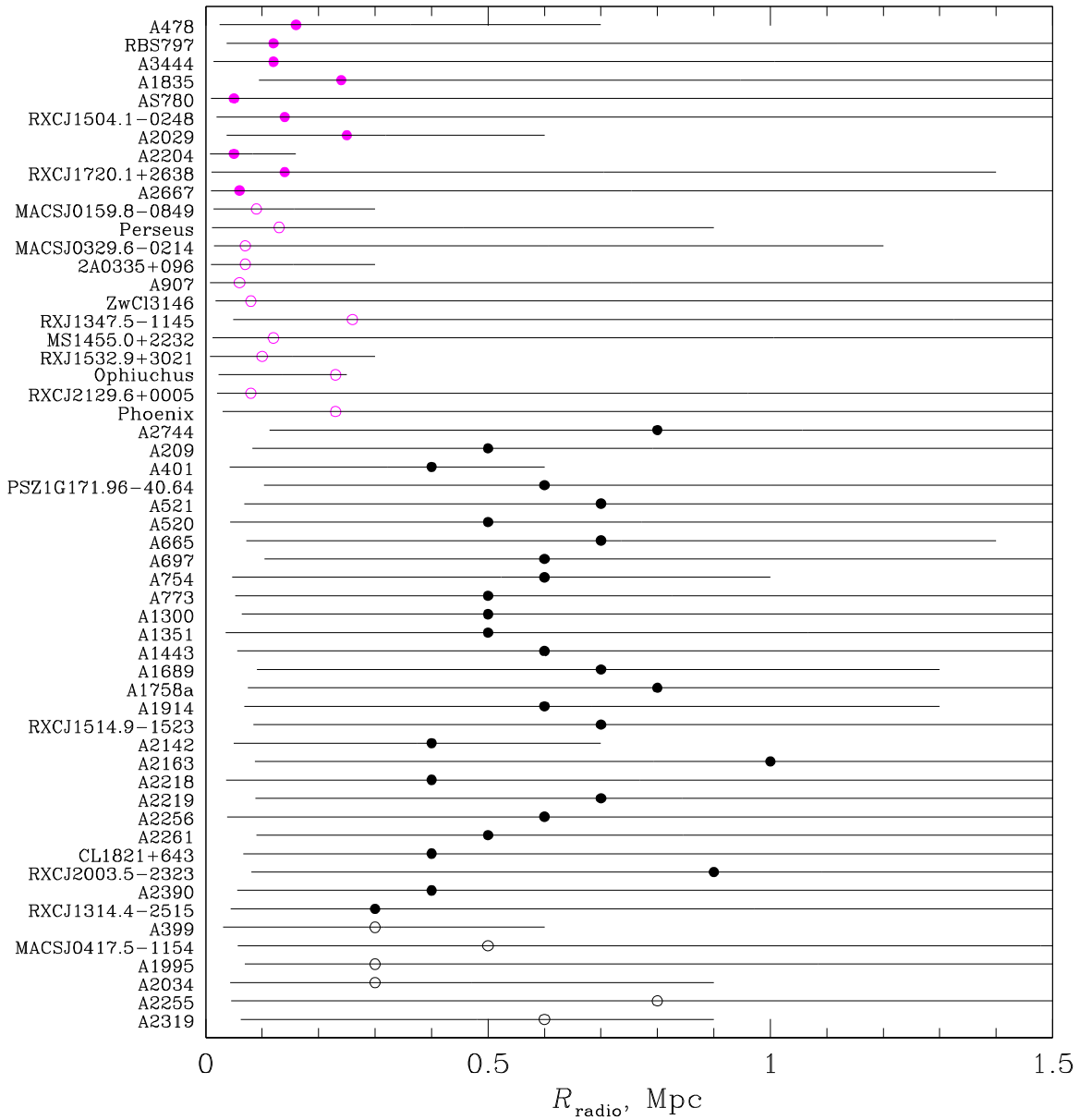

Figure 12. Radius of minihalos (magenta) and halos (black) in the statistical sample (filled symbols) and supplementary sample (empty symbols). Horizontal lines show the range of linear scales that can be detected in the corresponding radio images: the minimum scale is the angular resolution of the image, the maximum scale is the radius of the largest structure that can be imaged by the observations (Table 10).

A.1. Notes on Individual Clusters

A193. The combined C- and D-configuration image (Figure 9, right upper panel) shows a central double radio source with a flux density of 61 ± 3 mJy. The combined C-configuration image (Figure 9, left upper panel) reveals the source to be composed of a bright compact component, coincident with the cluster central galaxy, and a ∼60 kpc long "tail" toward the northeast (see also Owen et al. 1993; Owen & Ledlow 1997). The total flux in this image is 60 ± 3 mJy, of which 28 ± 1 mJy is in the compact component.

A383. A single point source with 41 ± 2 mJy is detected at cluster central galaxy in all our images (Figure 9, middle panels). Its size is <5 kpc, based on a Gaussian fit on our highest resolution image, obtained from the combination of the A-configuration observations.

MS 0440.5+0204. A central extended radio source is detected in the C-configuration image (Figure 9, bottom panels). At the higher resolution of the A-configuration observation, the source separates into a ∼30 kpc double, associated with the cluster central galaxy, and a head–tail radio galaxy, identified as a member galaxy ($z = 0.193$, Gioia et al. 1998). A total flux of 43.6 ± 2.2 mJy is measured on the C-configuration image. This value is consistent with the sum of the flux densities in the double (33.0 ± 1.7 mJy) and head–tail (10.6 ± 0.5 mJy) measured at higher resolution.

MACS J0429.6−0253. An unresolved source is detected at the cluster center in both A- and B-configuration images (Figure 10, left upper panel; see also Figure 7), with flux densities of 133 ± 7 mJy and 138 ± 7 mJy, respectively. Based on the A-configuration image, the source is <10 kpc in size.

MS 0839.8+2938. The C-configuration observation detects a central compact radio source, which the B-configuration reveals to be an 80 kpc long, core-dominated double radio

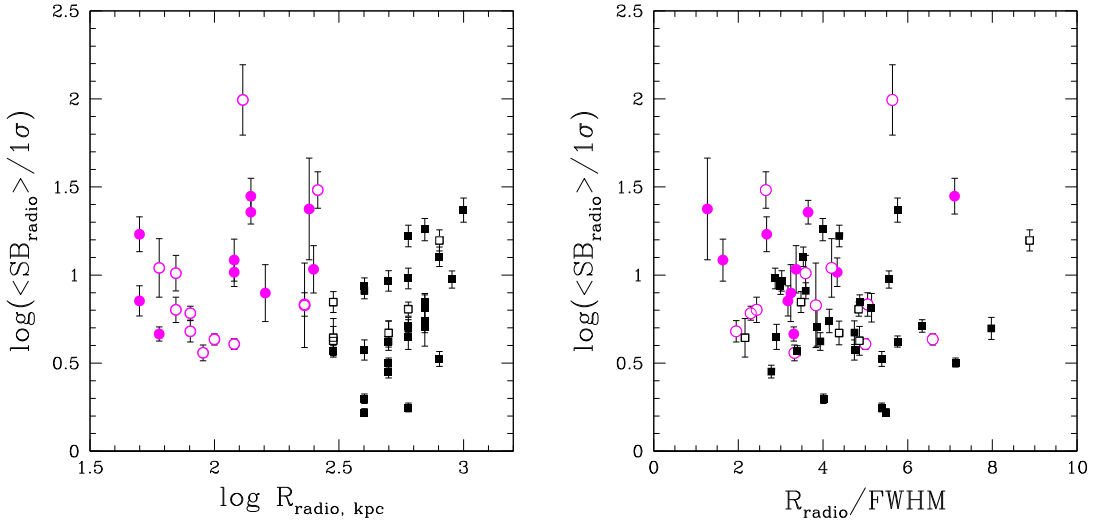

Figure 13. Ratios of the average surface brightness of minihalos (magenta) and large halos (black) to the rms noise level (per beam) of the corresponding radio images (Table 10). The ratios are plotted as a function of the radius in kiloparsecs (left) and beam sizes (right). Filled symbols are clusters in the statistical sample and empty symbols are those in the supplementary sample.

source (Figure 10, right upper panel; see also Figure 7). Its flux density is 26 ± 1 mJy (C configuration) and 25 ± 1 mJy (B configuration).

A1204. An unresolved source (size < 40 kpc) is detected at the cluster center in the C-configuration image (Figure 10, middle panels). Its flux density is 1.8 ± 0.1 mJy. An unresolved source is also detected by a slightly higher-resolution observation at 5 GHz with the VLA in C configuration (Hogan et al. 2015), with a similar flux of 1.8 mJy, implying a flat spectral index between 1.4 and 5 GHz.

A2125. A deep radio survey of the cluster region has been carried out by Owen et al. (2005) using the VLA at 1.4 GHz in its A and B configurations. An image of the central cluster region is presented in Owen et al. (2006). The region is occupied by a triple system of optical galaxies, each hosting an extended radio source, and a nearby bright compact radio galaxy, named C153. Here we present a lower-resolution image of the cluster center, obtained from an archival VLA observation in C configuration (Figure 10, bottom panels). The three central sources, individually detected by Owen et al., appear here blended into a single source with a total flux density of 19 ± 1 mJy. This value is in agreement with the sum of the flux densities measured by Owen et al. (2005) for these three sources (19.3 mJy). C153 is unresolved in our image; its flux density of 22.9 ± 0.7 mJy is in good agreement with that reported by Owen et al. (22.9 mJy).

A2420. A slightly extended radio source, oriented north–south and with a flux density of 198 ± 10 mJy, is detected at the position of the central galaxy in the CnB-configuration image (Figure 11, left upper panel). In the DnC-configuration image (Figure 11, right upper panel), the source has a flux of 197 ± 10 mJy. The compact radio galaxy visible to the northeast has a flux of 1.5 ± 0.1 mJy (CnB configuration) and 2.1 ± 0.1 mJy (DnC configuration).

A2556. The CnB-configuration and combined CnB+DnC-configuration images (Figure 11, bottom panels) show an extended radio source associated with the dominant cluster galaxy, with a size of ∼65 kpc along the NE–SW axis. A radio galaxy with head–tail morphology is located at a projected distance of about 90 kpc from the central galaxy. The flux densities of these sources, measured on the combined image are 1.9 ± 0.1 mJy and 20 ± 1 mJy, respectively. The two radio galaxies are blended together in the lower-resolution image from the DnC configuration (Figure 11, left bottom panel) with a total flux density of 22 ± 1 mJy.

Appendix B
Radio Size and Average Surface Brightness of Minihalos and Halos

In Table 10 we summarize the properties—frequency, angular resolution, sensitivity, and the radius of the largest detectable structure (based on full-synthesis nominal values for GMRT, VLA, and WSRT)—of the radio images used to estimate the extent of the radio sources in our statistical and supplementary samples (candidates are not included). For each source, the table also lists the measured radius (the average radius of a 3σ isocontour, Section 2) and the ratio of the average surface brightness of the source to the rms noise level of the corresponding radio image.

In Figure 12, we compare the measured source radii to the interval of linear scales that can be detected in the respective radio images. The minimum scale is set by the angular resolution of the image (average FWHM, Table 10). We note here that almost all clusters have complementary observations at higher resolution. The maximum scale is the radius of the largest structure that can be detected in this particular observation (Table 10). Even though the actual scale that can be reliably imaged by the observation can be less than the nominal value (due, for instance, to a short exposure or to the exclusion of bad data at short baselines), the minihalo and halo radii are typically much less than LDS/2 (one exception is Ophiuchus). This indicates that the observations are not limited by the interferometric coverage; if there was emission outside the minihalo, and provided the noise was sufficiently low, then we should be able to detect it well beyond the cool core, and in most cases on scales comparable to those of large halos. The other obvious instrumental limitation is the noise level—if minihalos and large halos were similar sources with a smoothly declining radial brightness profile, a more sensitive observation would yield a larger radius of the 3σ isophote. In Figure 13, we show the ratio of the average surface brightness of the source to

the image rms noise (Table 10) as a function of the radius in kiloparsecs (left panel) or in beam sizes (right panel). There is no correlation between the signal-to-noise ratio and the radius of the halo; the signal-to-noise ratios for the minihalos are similar to those for the large halos and in several cases even slightly higher. This is in agreement with a similar plot for giant halos in Cassano et al. (2007). Based on Figures 12 and 13, we conclude that most of the minihalo data sets used in this work possess the requisite sensitivity to detect diffuse emission on angular scales greater than the minihalo at a surface brightness level typical of large halos, thus the measured difference between the sizes of minihalos and large halos is physically meaningful. This answers a frequently asked question of whether minihalos are simply the peaks of larger halos in a cluster with the central density peak (and where the radio emission roughly follows the ICM density)—in such a picture, we would be able to detect the rest of the halo emission outside the cool core, and we do not.

References

Andrade-Santos, F., Jones, C., Forman, W., et al. 2017, ApJ, submitted (arXiv:1703.08690)
Ascasibar, Y., & Markevitch, M. 2006, ApJ, 650, 102
Bacchi, M., Feretti, L., Giovannini, G., & Govoni, F. 2003, A&A, 400, 465
Barrena, R., Boschin, W., Girardi, M., & Spolaor, M. 2007, A&A, 469, 861
Bonafede, A., Giovannini, G., Feretti, L., Govoni, F., & Murgia, M. 2009, A&A, 494, 429
Bonafede, A., Intema, H., Brüggen, M., et al. 2015, MNRAS, 454, 3391
Bonafede, A., Intema, H. T., Brüggen, M., et al. 2014, MNRAS, 444, L44
Bravi, L., Gitti, M., & Brunetti, G. 2016, MNRAS, 455, L41
Brentjens, M. A. 2008, A&A, 489, 69
Briggs, D. S. 1995, BAAS, 27, 112.02
Brunetti, G., Giacintucci, S., Cassano, R., et al. 2008, Natur, 455, 944
Brunetti, G., & Jones, T. W. 2014, IJMPD, 23, 1430007
Burns, J. O., Sulkanen, M. E., Gisler, G. R., & Perley, R. A. 1992, ApJL, 388, L49
Cassano, R., & Brunetti, G. 2005, MNRAS, 357, 1313
Cassano, R., Brunetti, G., Giocoli, C., & Ettori, S. 2016, A&A, 593, A81
Cassano, R., Brunetti, G., & Setti, G. 2006, MNRAS, 369, 1577
Cassano, R., Brunetti, G., Setti, G., Govoni, F., & Dolag, K. 2007, MNRAS, 378, 1565
Cassano, R., Ettori, S., Brunetti, G., et al. 2013, ApJ, 777, 141
Cassano, R., Ettori, S., Giacintucci, S., et al. 2010, ApJL, 721, L82
Cassano, R., Gitti, M., & Brunetti, G. 2008, A&A, 486, L31
Cavagnolo, K. W., Donahue, M., Voit, G. M., & Sun, M. 2008, ApJ, 682, 821 (C08)
Cavagnolo, K. W., Donahue, M., Voit, G. M., & Sun, M. 2009, ApJS, 182, 12 (C09)
Cavaliere, A., & Fusco-Femiano, R. 1978, A&A, 70, 677
Clarke, T. E., & Ensslin, T. A. 2006, AJ, 131, 2900
Crawford, C. S., Allen, S. W., Ebeling, H., Edge, A. C., & Fabian, A. C. 1999, MNRAS, 306, 857
Cuciti, V., Cassano, R., Brunetti, G., et al. 2015, A&A, 580, A97
Dallacasa, D., Brunetti, G., Giacintucci, S., et al. 2009, ApJ, 699, 1288
David, L. P., Slyz, A., Jones, C., et al. 1993, ApJ, 412, 479
Doria, A., Gitti, M., Ettori, S., et al. 2012, ApJ, 753, 47
Ehlert, S., Allen, S. W., von der Linden, A., et al. 2011, MNRAS, 411, 1641
Farnsworth, D., Rudnick, L., Brown, S., & Brunetti, G. 2013, ApJ, 779, 189
Feretti, L., Boehringer, H., Giovannini, G., & Neumann, D. 1997, A&A, 317, 432
Feretti, L., Fusco-Femiano, R., Giovannini, G., & Govoni, F. 2001, A&A, 373, 106
Feretti, L., Giovannini, G., & Boehringer, H. 1997, NewA, 2, 501
Feretti, L., Giovannini, G., Govoni, F., & Murgia, M. 2012, A&ARv, 20, 54
Feretti, L., Schuecker, P., Böhringer, H., Govoni, F., & Giovannini, G. 2005, A&A, 444, 157
Ferrari, C., Intema, H. T., Orrù, E., et al. 2011, A&A, 534, L12
Fujita, Y., Kohri, K., Yamazaki, R., & Kino, M. 2007, ApJL, 663, L61
Fujita, Y., & Ohira, Y. 2011, ApJ, 738, 182
Fujita, Y., & Ohira, Y. 2013, MNRAS, 428, 599
Gendron-Marsolais, M., Hlavacek-Larrondo, J., van Weeren, R. J., et al. 2017, MNRAS, submitted (arXiv:1701.03791)
Giacintucci, S., Dallacasa, D., Venturi, T., et al. 2011a, A&A, 534, A57
Giacintucci, S., Kale, R., Wik, D. R., Venturi, T., & Markevitch, M. 2013, ApJ, 770, 161
Giacintucci, S., Markevitch, M., Brunetti, G., et al. 2014a, ApJ, 795, 73
Giacintucci, S., Markevitch, M., Brunetti, G., Cassano, R., & Venturi, T. 2011b, A&A, 525, L10
Giacintucci, S., Markevitch, M., Venturi, T., et al. 2014b, ApJ, 781, 9
Giacintucci, S., Venturi, T., Brunetti, G., et al. 2009, A&A, 505, 45
Giacintucci, S., Venturi, T., Cassano, R., Dallacasa, D., & Brunetti, G. 2009, ApJL, 704, L54
Gioia, I. M., Shaya, E. J., Le Fèvre, O., et al. 1998, ApJ, 497, 573
Giovannini, G., Bonafede, A., Feretti, L., et al. 2009, A&A, 507, 1257
Giovannini, G., & Feretti, L. 2000, NewA, 5, 335
Gitti, M. 2013, MNRAS, 436, L84
Gitti, M., Brunetti, G., Feretti, L., & Setti, G. 2004, A&A, 417, 1
Gitti, M., Brunetti, G., & Setti, G. 2002, A&A, 386, 456
Gitti, M., Feretti, L., & Schindler, S. 2006, A&A, 448, 853
Gitti, M., Ferrari, C., Domainko, W., Feretti, L., & Schindler, S. 2007, A&A, 470, L25
Gitti, M., Tozzi, P., Brunetti, G., et al. 2015, in Advancing Astrophysics with the Square Kilometre Array (Trieste: PoS), 76
Govoni, F., Feretti, L., Giovannini, G., et al. 2001, A&A, 376, 803
Govoni, F., Murgia, M., Feretti, L., et al. 2005, A&A, 430, L5
Govoni, F., Murgia, M., Giovannini, G., Vacca, V., & Bonafede, A. 2011, A&A, 529, A69
Govoni, F., Murgia, M., Markevitch, M., et al. 2009, A&A, 499, 371
Guo, F., & Oh, S. P. 2008, MNRAS, 384, 251
Hitomi Collaboration, Aharonian, F., Akamatsu, H., et al. 2016, Natur, 535, 117
Hlavacek-Larrondo, J., Allen, S. W., Taylor, G. B., et al. 2013, ApJ, 777, 163
Hogan, M. T., Edge, A. C., Hlavacek-Larrondo, J., et al. 2015, MNRAS, 453, 1201
Ikebe, Y., Reiprich, T. H., Böhringer, H., Tanaka, Y., & Kitayama, T. 2002, A&A, 383, 773
Jacob, S., & Pfrommer, C. 2017a, MNRAS, 467, 1478
Jacob, S., & Pfrommer, C. 2017b, MNRAS, 467, 1449
Jones, C., & Forman, W. 1984, ApJ, 276, 38
Kalberla, P. M. W., Burton, W. B., Hartmann, D., et al. 2005, A&A, 440, 775
Kale, R., & Parekh, V. 2016, MNRAS, 459, 2940
Kale, R., Venturi, T., Giacintucci, S., et al. 2013, A&A, 557, A99
Kale, R., Venturi, T., Giacintucci, S., et al. 2015, A&A, 579, A92
Kassim, N. E., Clarke, T. E., Enßlin, T. A., Cohen, A. S., & Neumann, D. M. 2001, ApJ, 559, 785
Macario, G., Intema, H. T., Ferrari, C., et al. 2014, A&A, 565, A13
Macario, G., Markevitch, M., Giacintucci, S., et al. 2011, ApJ, 728, 82
Macario, G., Venturi, T., Brunetti, G., et al. 2010, A&A, 517, A43
Macario, G., Venturi, T., Intema, H. T., et al. 2013, A&A, 551, A141
Markevitch, M., Mazzotta, P., Vikhlinin, A., et al. 2003, ApJL, 586, L19
Markevitch, M., Ponman, T. J., Nulsen, P. E. J., et al. 2000, ApJ, 541, 542
Mazzotta, P., & Giacintucci, S. 2008, ApJL, 675, L9
Mazzotta, P., Rasia, E., Moscardini, L., & Tormen, G. 2004, MNRAS, 354, 10
McDonald, M., Allen, S. W., Bayliss, M., et al. 2017, ApJ, submitted (arXiv:1702.05094)
McDonald, M., McNamara, B. R., van Weeren, R. J., et al. 2015, ApJ, 811, 111
McNamara, B. R., & Nulsen, P. E. J. 2007, ARA&A, 45, 117
Mittal, R., Hudson, D. S., Reiprich, T. H., & Clarke, T. 2009, A&A, 501, 835
Murgia, M., Eckert, D., Govoni, F., et al. 2010a, A&A, 514, A76
Murgia, M., Govoni, F., Feretti, L., & Giovannini, G. 2010b, A&A, 509, A86
Murgia, M., Govoni, F., Markevitch, M., et al. 2009, A&A, 499, 679
Murgia, M., Markevitch, M., Govoni, F., et al. 2012, A&A, 548, A75
Murgia, M., Parma, P., Mack, K.-H., et al. 2011, A&A, 526, A148
Nagai, D. 2006, ApJ, 650, 538
Owen, F. N., Keel, W. C., Wang, Q. D., Ledlow, M. J., & Morrison, G. E. 2006, AJ, 131, 1974
Owen, F. N., & Ledlow, M. J. 1997, ApJS, 108, 41
Owen, F. N., Ledlow, M. J., Keel, W. C., Wang, Q. D., & Morrison, G. E. 2005, AJ, 129, 31
Owen, F. N., White, R. A., & Ge, J. 1993, ApJS, 87, 135
Pandey-Pommier, M., Richard, J., Combes, F., et al. 2016, in Proc. Annual Meeting of the French Society of Astronomy and Astrophysics, SF2A-2016, ed. C. Reylé et al. (Paris: SF2A), 367

Parekh, V., Dwarakanath, K. S., Kale, R., & Intema, H. 2017, MNRAS, 464, 2752
Parekh, V., van der Heyden, K., Ferrari, C., Angus, G., & Holwerda, B. 2015, A&A, 575, A127
Perley, R. A., & Butler, B. J. 2013, ApJS, 204, 19
Pfrommer, C., & Enßlin, T. A. 2004, A&A, 413, 17
Pizzo, R. F., & de Bruyn, A. G. 2009, A&A, 507, 639
Planck Collaboration, Ade, P. A. R., Aghanim, N., et al. 2014, A&A, 571, 29
Reid, A. D., Hunstead, R. W., Lemonon, L., & Pierre, M. M. 1999, MNRAS, 302, 571
Rossetti, M., Eckert, D., De Grandi, S., et al. 2013, A&A, 556, A44
Rossetti, M., Gastaldello, F., Ferioli, G., et al. 2016, MNRAS, 457, 4515
Saikia, D. J., & Jamrozy, M. 2009, BASI, 37, 63
Sarazin, C. L., Baum, S. A., & O'Dea, C. P. 1995, ApJ, 451, 125
Sijbring, L. G. 1993, PhD thesis, Univ. Groningen
Sommer, M. W., Basu, K., Intema, H., et al. 2017, MNRAS, 466, 996
Storm, E., Jeltema, T. E., & Rudnick, L. 2015, MNRAS, 448, 2495
Vacca, V., Feretti, L., Giovannini, G., et al. 2014, A&A, 561, A52
Vacca, V., Govoni, F., Murgia, M., et al. 2011, A&A, 535, A82
van Weeren, R. J., Intema, H. T., Lal, D. V., et al. 2014, ApJL, 786, L17
van Weeren, R. J., Röttgering, H. J. A., Brüggen, M., & Hoeft, M. 2010, Sci, 330, 347
Venturi, T., Giacintucci, G., Dallacasa, D., et al. 2011, MNRAS, 414, L65
Venturi, T., Giacintucci, S., Brunetti, G., et al. 2007, A&A, 463, 937
Venturi, T., Giacintucci, S., Dallacasa, D., et al. 2008, A&A, 484, 327
Venturi, T., Giacintucci, S., & Dallacasa, D. 2011, JApA, 32, 501
Venturi, T., Giacintucci, S., Dallacasa, D., et al. 2013, A&A, 551, A24
Venturi, T., Rossetti, M., & Brunetti, G. 2017, A&A, in press (arXiv:1703.06802)
Vikhlinin, A., Burenin, R. A., Ebeling, H., et al. 2009, ApJ, 692, 1033
Vikhlinin, A., Kravtsov, A., Forman, W., et al. 2006, ApJ, 640, 691
Vikhlinin, A., Markevitch, M., Murray, S. S., et al. 2005, ApJ, 628, 655
White, D. A., Jones, C., & Forman, W. 1997, MNRAS, 292, 419
Yuan, Z. S., Han, J. L., & Wen, Z. L. 2015, ApJ, 813, 77
Zandanel, F., Pfrommer, C., & Prada, F. 2014, MNRAS, 438, 124
Zhuravleva, I., Churazov, E., Schekochihin, A. A., et al. 2014, Natur, 515, 85
ZuHone, J. A., Markevitch, M., Brunetti, G., & Giacintucci, S. 2013, ApJ, 762, 78